

# ON SIZES, KINEMATICS, M/L GRADIENTS, AND LIGHT PROFILES OF MASSIVE COMPACT GALAXIES AT $Z \sim 2$

STIJN WUYTS<sup>1,2</sup>, THOMAS J. COX<sup>3</sup>, CHRISTOPHER C. HAYWARD<sup>1</sup>, MARIJN FRANX<sup>4</sup>, LARS HERNQUIST<sup>1</sup>, PHILIP F. HOPKINS<sup>5</sup>, PATRIK JONSSON<sup>1,2</sup>, PIETER G. VAN DOKKUM<sup>6</sup>

*Draft version August 26, 2010*

## ABSTRACT

We present a detailed analysis of the structure and resolved stellar populations of simulated merger remnants, and compare them to observations of compact quiescent galaxies at  $z \sim 2$ . We find that major merging is a viable mechanism to produce systems of  $\sim 10^{11} M_{\odot}$  and  $\sim 1$  kpc size, provided the gas fraction at the time of final coalescence is high ( $\sim 40\%$ ), and provided that the progenitors are compact star-forming galaxies, as expected at high redshift. Their integrated spectral energy distributions and velocity dispersions are in good agreement with the observations, and their position in the  $(v_{\text{maj}}/\sigma, \epsilon)$  diagram traces the upper envelope of the distribution of lower redshift early-type galaxies. The simulated merger remnants show time- and sightline-dependent  $M/L$  ratio gradients that result from a superposition of radially dependent stellar age, stellar metallicity, and extinction. The median ratio of effective radius in rest-frame  $V$ -band light to that in mass surface density is  $\sim 2$  during the quiescent remnant phase. This is typically expressed by a negative color gradient (i.e., red core), which we expect to correlate with the integrated color of the system. Finally, the simulations differ from the observations in their surface brightness profile shape. The simulated remnants are typically best fit by high ( $n \gg 4$ ) Sersic indices, whereas observed quiescent galaxies at  $z \sim 2$  tend to be less cuspy ( $\langle n \rangle \sim 2.3$ ). Limiting early star formation in the progenitors may be required to prevent the simulated merger remnants from having extended wings.

*Subject headings:* galaxies: evolution, galaxies: formation - galaxies: structure - galaxies: stellar content

## 1. INTRODUCTION

Recent surveys of the high-redshift universe have identified a substantial population of massive quiescent galaxies, already in place at  $z \geq 2$  (e.g., Labbé et al. 2005; Daddi et al. 2005; van Dokkum et al. 2006; Kriek et al. 2006). Studies of their structural parameters have convincingly ruled out simple monolithic collapse models, in which little to no structural evolution is expected. Instead, observational studies find galaxies, and especially quiescent galaxies, to grow significantly in size as time progresses (e.g., Trujillo et al. 2006; Toft et al. 2007; Zirm et al. 2007; van Dokkum et al. 2008; Cimatti et al. 2008; van der Wel et al. 2008; Franx et al. 2008; Buitrago et al. 2008). At  $z \sim 2.3$ , massive quiescent galaxies are typically 5 times more compact, and two orders of magnitude more dense than local ellipticals of the same mass (e.g., van Dokkum et al. 2008, hereafter vD08). Bezanson et al. (2009) note that, even though their effective densities (measured within one effective radius  $r_e$ ) are strikingly high compared to local ellipticals, the central densities measured within a fixed aperture of 1 kpc exceed those of local ellipticals by no more than a factor 2-3 (see also Hopkins et al. 2009d). This obser-

vation suggests an inside-out growth, in agreement with stacking results by van Dokkum et al. (2010).

Motivated by these recent observational developments, several mechanisms have been proposed to incorporate the constraints on structural evolution into galaxy formation theories. In most cases, minor and/or major mergers are invoked to explain the observed size evolution (Khochfar & Silk 2006a; Naab et al. 2007, 2009; Hopkins et al. 2009a). Briefly, mergers were more gas-rich at high redshifts, and hence formed a larger fraction of their stars in a nuclear dissipational component, explaining their compact nature. Subsequent (dry) merging activity puffs up the system without adding too much mass or new stars, which would violate observational constraints. However, alternative scenarios involving an expansion of the stellar distribution as response to significant mass losses have been suggested as well (Fan et al. 2008). In either case, an accurate observational characterization of the size-mass relation provides a crucial test for galaxy formation models.

Given the paucity of kinematic mass measurements based on absorption-line spectra of  $z > 1.5$  galaxies (although see Cenarro & Trujillo 2009; Cappellari et al. 2009; van Dokkum, Kriek & Franx 2009), studies of the high-redshift size-mass scaling relation to date have focussed on stellar mass estimates from spectral energy distribution (SED) modeling (e.g., Williams et al. 2010). Significant systematic uncertainties related to the assumption of an IMF (e.g., van Dokkum 2008; Davé 2008; Wilkins et al. 2008) and the choice of a stellar population synthesis code (e.g., Maraston et al. 2006; Wuyts et al. 2007; Muzzin et al. 2009a) remain. Uncertainties related to the star formation history, metallicity, and dust

<sup>1</sup> Harvard-Smithsonian Center for Astrophysics, 60 Garden Street, Cambridge, MA 02138

<sup>2</sup> W. M. Keck Postdoctoral Fellow

<sup>3</sup> Carnegie Observatories, 813 Santa Barbara Street, Pasadena, CA 91101

<sup>4</sup> Leiden University, Leiden Observatory, P.O. Box 9513, NL-2300 RA, Leiden, The Netherlands.

<sup>5</sup> Department of Astronomy, University of California Berkeley, Berkeley, CA 94720

<sup>6</sup> Department of Astronomy, Yale University, New Haven, CT 06520-8101

attenuation are relatively modest for the quiescent population, they only contribute significantly to the overall uncertainty during earlier, actively star-forming phases (Wuyts et al. 2009a). However important an accurate characterization of mass, we focus in this paper on the measurement of the second parameter of the scaling relation: galaxy size.

Observations probe the projected distribution of light, sampling it by a discrete number of pixels after it was smeared by a point spread function (PSF). In addition, the signal is superposed by noise. The translation to a physically more meaningful mass profile involves the assumption of a mass-to-light ratio  $M/L$ . Although often for simplicity assumed to be a constant, spatial variations in  $M/L$  may occur due to age, metallicity and/or dust gradients. Furthermore, since the total size of a galaxy is ill-defined, one refers to (circularized) size as the radius  $r_e$  containing half the mass. Given the finite image resolution, this quantity is generally obtained by fitting a template profile, taking pixelization and PSF smearing into account. In most of the literature, a one-component Sersic (1968) profile has been adopted, providing satisfyingly flat residual images given the noise level of the observations.

Numerical simulations provide an excellent tool for the interpretation of galaxy structure. The simulated data offers a three-dimensional view of the mass, age, and metallicity profile at high resolution, free of sky noise<sup>1</sup>. By feeding the output to a radiative transfer code and producing mock observations, each of the above aspects related to the nature of observational data can be isolated, and its effect analyzed. For example, contrasting the light profiles of local gas-rich merger remnants and ellipticals with those of simulated merger remnants, Hopkins et al. (2008b, 2009b) demonstrated that a two-component profile (consisting of an inner dissipational, and outer violently relaxed component) provides both a better fit and a physically more meaningful interpretation of their structure than a single Sersic profile.

In this paper, we compare the structure of simulated merger remnants to the best observations of compact quiescent galaxies at  $z \sim 2$  to date. In addition, we discuss the presence of  $M/L$  ratio gradients that may bias measurements of the half-mass radius, and can be revealed by multi-wavelength structural studies with the high-resolution cameras onboard *Hubble Space Telescope*. This study complements the comparison between observations and merger simulations by Wuyts et al. (2009b) that focussed on the integrated colors, number and mass densities of high-redshift quiescent galaxies.

We describe the simulations, and mock observations based thereupon in §2. There, we also caution for artificial heating in simulating regimes of extreme density. We discuss the relation between size and mass for quiescent galaxies with a range of formation histories in §3, and address their kinematics in §4. Next, we analyze radial variations in the  $M/L$  ratio, their origin in terms of stellar populations, and color gradients through which they manifest themselves (§5). Finally, we exploit realistic mock observations of the simulations to fit their surface

brightness profiles alongside real high-redshift compact galaxies. §6 highlights the cuspieness of the simulated profiles, and explores possible origins of an apparent profile mismatch with respect to the observations. We summarize the results in §7.

Throughout this paper, we adopt the following cosmological parameters:  $(\Omega_M, \Omega_\Lambda, h) = (0.3, 0.7, 0.7)$ .

## 2. THE SIMULATIONS

### 2.1. Main characteristics

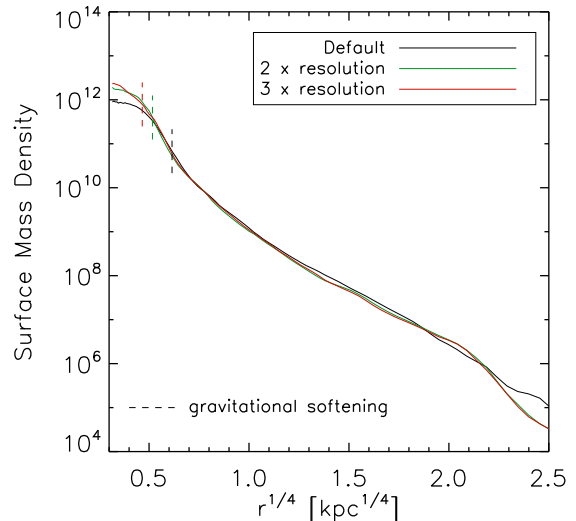


FIG. 1.— Surface mass density profiles of a compact merger remnant with final stellar mass of  $1.7 \times 10^{11} M_\odot$ , simulated with 1, 2, and 3 times the default spatial resolution adopted in this paper. The profiles are converged outside of a softening length.

This work is based on a suite of smoothed particle hydrodynamic (SPH) simulations representing isolated and merging galaxies at redshifts  $z \sim 0$  to 3 that were performed with the GADGET-2 code (Springel 2005). The code uses an entropy-conserving formalism of SPH (Springel & Hernquist 2002), and includes gas cooling, a multi-phase model for the interstellar medium (ISM) to describe star formation and supernova feedback (Springel & Hernquist 2003), and a prescription for supermassive black hole growth and feedback (Springel, Di Matteo & Hernquist 2005; Di Matteo, Springel & Hernquist 2005).

The progenitor disks in our simulations are embedded in an extended dark matter halo with a Hernquist (1990) profile. They span a range of baryonic masses from  $7 \times 10^9 M_\odot$  to  $4 \times 10^{11} M_\odot$ , and initial gas fractions of 20 - 80%. We mostly focus on the subset of massive gas-rich merger simulations in which the progenitors were scaled to approximate the structure of disk galaxies at redshift  $z = 3$ , following Robertson et al. (2006). Briefly, this means that the mass- and redshift-dependent halo concentration measured by Bullock et al. (2001) was adopted:

$$C_{vir}(M_{vir}, z) \approx 9 \left( \frac{M_{vir}}{M_{coll,0}} \right)^{-0.13} (1+z)^{-1}, \quad (1)$$

where  $M_{coll,0} \sim 8 \times 10^{12} h^{-1} M_\odot$  is the linear collapse mass at  $z=0$ . The virial mass and virial radius of the progenitors were scaled as follows:

$$M_{vir} = \frac{V_{vir}^3}{10GH(z)} \quad (2)$$

<sup>1</sup> The finite number of particles introduces particle noise, but for the simulations analyzed in this paper this is negligible on the scales we study.

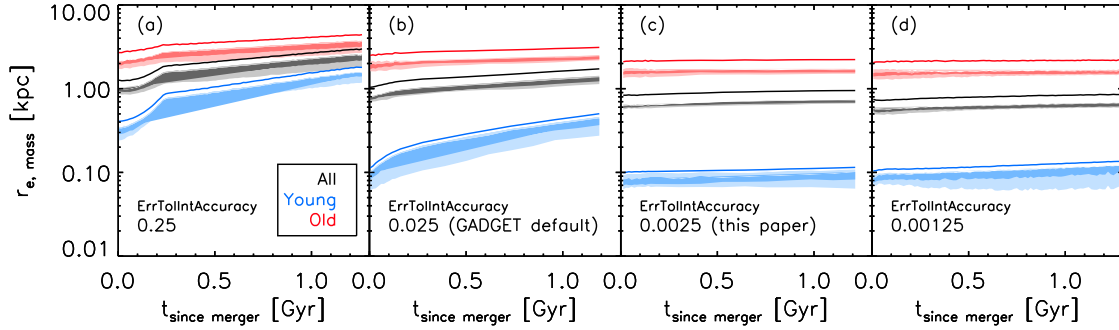


FIG. 2.— Size evolution after final coalescence of a compact merger remnant with a final stellar mass of  $1.7 \times 10^{11} M_{\odot}$ . The top line for each color-coded component indicates the 3D half-mass radius, whereas the light (dark) polygon below illustrates the full (central 50-percentile) range of 2D projected half-mass radii of the system as viewed from different sightlines. Panels (a) to (d) represent realizations of SPH simulations with increasingly finer timestep resolution and otherwise identical conditions. Numerical heating causes an artificial increase in size when the orbital paths of SPH particles in a dense environment are integrated with insufficient resolution. For a system of  $\sim 10^{11} M_{\odot}$  and half-mass radius of  $\sim 1$  kpc, the size evolution is not yet converged for the default GADGET timestep resolution.

$$R_{vir} = \frac{V_{vir}}{10H(z)}, \quad (3)$$

where  $V_{vir}$  is the virial velocity and  $H(z)$  is the Hubble parameter. Disk sizes were initialized according to the Mo et al. (1998) formalism for dissipational disk galaxy formation assuming the fraction of the total angular momentum contained in the disk equals the fraction of the total mass contained in the disk. The disk scale length is then derived from the halo concentration  $C_{vir}$  (Eq. 1) and the galaxy spin  $\lambda$ , where we adopt a default  $\lambda = 0.033$ , as motivated by cosmological N-body simulations (Vitvitska et al. 2002). In practice, this means that the  $z = 3$ -scaled progenitor disks have effective radii that are a factor 1.7 smaller than similar mass galaxies today, in agreement with the observed size evolution of star-forming galaxies (Franx et al. 2008).

Equal-mass mergers were simulated for a range of orbital configurations, from coplanar to polar to various tilted disk orientations, following Cox et al. (2006). Specifically, we analyzed simulations with the range of spin axis orientations of the progenitor disks listed, in standard spherical coordinates, in Table 1. In typical runs, each of the two progenitor galaxies initially consists of 60000 to 120000 dark matter particles, 40000 gas and 40000 stellar disk particles, and one black hole sink particle. For the mass range probed by our simulations, this corresponds to typical mass resolutions of the baryonic and dark matter particles of  $M_{bar} = 1 - 8 \times 10^5 M_{\odot}$  and  $M_{DM} = 0.5 - 4 \times 10^7 M_{\odot}$  respectively. In addition to equal-mass mergers, we also ran simulations in which the disk galaxy was left to evolve in isolation, simulations of unequal-mass mergers, and scenarios where a merger remnant undergoes subsequent merging.

We adopted a gravitational softening length of  $\epsilon = 140$  pc. A resolution study for one of our fiducial merger simulations, where we increased the mass resolution by a factor 4 and repeated the simulations with two and three times the spatial resolution (i.e., adopting softening lengths that are half or a third of our default) and otherwise identical conditions confirms that the adopted resolution is sufficient for the purposes of this paper (Figure 1). The total stellar mass of the merger remnant

TABLE 1. DISK ORIENTATIONS

ID <sup>a</sup>	$\theta_1$	$\phi_1$	$\theta_2$	$\phi_2$	Comments
h	0	0	0	0	both prograde
b	180	0	0	0	prograde-retrograde
d	90	0	0	0	polar
e	30	60	-30	45	tilted 1
g	150	0	-30	45	tilted 2
i	0	0	71	30	Barnes orientations <sup>b</sup>
j	-109	90	71	90	↓
k	-109	-30	71	-30	
l	-109	30	180	0	
m	0	0	71	90	
n	-109	-30	71	30	
o	-109	30	71	-30	
p	-109	90	180	0	

<sup>a</sup>Unique orientation identification from Cox et al. (2006).

<sup>b</sup>Selected by Barnes (1992) to be unbiased initial disk orientations according to the coordinates of two oppositely directed tetrahedra.

varies by a few percent only when increasing the spatial resolution. At radii larger than the softening length, the surface mass density profiles are converged at the 10% level. Within a radius of 140 pc, the amount of stellar mass assembled in the nucleus tends to be somewhat larger in the higher resolution runs. We furthermore refined the GADGET-2 timestep resolution by a factor  $\sqrt{10}$  with respect to the GADGET-2 default, resulting in runtimes that are longer by the same factor. Figure 2 illustrates the importance of the latter choice when studying (sub)structure at high spatial densities. The panels illustrate four realizations of a gas-rich merger simulation with a final stellar mass of  $1.7 \times 10^{11} M_{\odot}$  and half-light radius of  $\sim 1$  kpc, identical except for the timestep resolution with which particle orbits are integrated. The timestep scales with  $\sim \sqrt{\epsilon\eta}$ , where the respective value of the GADGET-2 parameter  $\eta = \text{ErrTolIntAccuracy}$  is shown in the panel. For each realization, we show the 3D (top line) and 2D (bottom polygon) half-mass radius evolution as function of time since the merger, which we define as the radius of a sphere (respectively circle) encompassing half of the (projected) stellar

mass. Throughout this paper, we define time of merging as the moment when the peak in star formation activity is reached. Different colors represent the size evolution of the galaxy as a whole (black), the young component of stars that formed within a 250 Myr interval around final coalescence (blue), and the old component of stars that were already formed prior to the nuclear starburst (red). Several conclusions can be drawn from Figure 2. First, numerical heating can lead to artificial growth of the simulated merger remnant. Since this effect is not uniform over the galaxy, but manifests itself particularly in the dense and young central component, it can also artificially alter the profile shape. Furthermore, the stellar mass formed during the nuclear starburst steadily decreases when a finer timestep resolution is adopted, by 26% when comparing simulation (a) to (d) from Figure 2, and by 10% when comparing simulation (b) to (d). This trend suggests that, in addition to artificial growth during the post-merger phase, the implementation of star formation and/or feedback processes may also depend on the length of the integration time step. This result has important implications for studies of structural evolution of massive galaxies based on cosmological simulations, where finite computational power imposes a delicate tradeoff between the box size (essential for reliable number statistics at the massive end), the spatial resolution, and the timestep resolution. Clearly, by compromising the timestep resolution to a level where no numerical convergence is reached, spurious growth in size and smoothing of cusps will be superposed on galaxy growth by real physical processes.

A second conclusion to draw from Figure 2 is that, once a converging timestep resolution is adopted, we find no evidence for size evolution after final coalescence in our binary merger simulations<sup>2</sup>. Third, the young dissipational component in this simulation that started with a gas fraction of 80% and was still very gas-rich ( $f_{\text{gas}} = 0.43$ ) at the time of final coalescence is more than an order of magnitude smaller than the old component of previously formed stars. Finally, by definition the 2D half-mass radius (which depends on viewing angle) is smaller than the 3D half-mass radius. We find a typical  $r_{e,3D}/r_{e,2D}$  ratio of 1.4. Furthermore, we find that the ratio  $r_{e,3D}/r_{e,2D}$  depends more strongly on viewing angle for the young component than for the old component, implying that the recent, dissipational star formation event took place in a disk-like structure, whereas the violently relaxed component has a more spherical shape. We find similar properties for the merger remnants produced by simulations that started with different orbital configurations.

## 2.2. Translating simulations to observables

The fluxes, colors and light profiles of the merger remnants are computed from the simulation output in two steps. First, the intrinsic stellar emission is derived from a stellar population synthesis code, where we treat each particle as a Simple Stellar Population (SSP) with its stellar mass, age and metallicity computed by the GADGET-2 code. We adopt a Kroupa (2001) IMF and

compute the photometry using Bruzual & Charlot (2003) or Maraston (2005) models. We find that our results are independent of the choice of stellar population synthesis code. Initial conditions (stellar age and metallicity) of the stellar and gas particles present at the start of the simulation were set by a simple closed box formalism detailed by Wuyts et al. (2009a). The precise choice of these initial stellar population properties has a negligible impact on the nature of the merger remnants that are the focus of this paper.

In step two, we use the information on the gas distribution and enrichment to compute the attenuating effect of dust on the emerging galaxy light. We perform our analysis using two independent codes that are frequently used in the literature. The first is a line-of-sight attenuation code (LOS) that simply computes the wavelength-dependent absorption to each stellar particle from the metallicity-weighted diffuse gas column density between that stellar particle and the observer (see Hopkins et al. 2005; Robertson et al. 2007; Wuyts et al. 2009a,b). The second code, SUNRISE (Jonsson 2006; Jonsson, Groves & Cox 2010), uses a Monte Carlo methodology to track photon packets on their way through the dusty ISM, and models the effects of both absorption and scattering. In addition, SUNRISE uses a sub-grid model to account for the attenuation by birth-clouds (HII and photodissociation regions) that surround young star clusters, computed using the photoionization code MAPPINGS (Groves et al. 2008). Furthermore, SUNRISE tracks dust temperatures and re-emission of absorbed light at longer wavelengths (see, e.g., Younger et al. 2009; Narayanan et al. 2010). However, since no high-resolution structural information is available in the far-infrared, and dust re-emission is negligible during the quiescent merger remnant phase, this aspect of the radiative transfer is not discussed in this paper. Likewise, the GADGET-2 simulation keeps track of gas accretion onto a central supermassive black hole, but its emission is negligible during the quiescent merger remnant phase of interest.

We compute realizations of the radiative transfer with attenuation laws representative of the Milky Way and the Small Magellanic Cloud. Unless specifically mentioned, our conclusions are qualitatively the same independent of the radiative transfer code or attenuation law used.

## 2.3. Mock images

We use the vD08 sample of compact quiescent galaxies at  $z \sim 2.3$  as reference. All 9 galaxies have a spectroscopically confirmed Balmer/4000Å break (Kriek et al. 2006). Seven of them were observed for 3 orbits in the F160W filter using the NIC2 camera on *HST*, probing their rest-frame optical emission. The two brightest galaxies were exposed for 2 orbits. At a drizzled pixel scale of  $0.0378''$ , the point-spread function (PSF) is well sampled, and the observations yielded the highest-resolution surface brightness maps of such galaxies to date.

In order to establish a fair comparison, we produce mock observations placing the simulated merger remnants at the same redshift, using the same observed filter and an identical pixel scale. We convolved the resulting postage stamps with a PSF extracted from the vD08 NIC2 images, applied Poisson noise, and added them into empty regions of the NIC2 images in order

<sup>2</sup> Note that this simulation does not include subsequent merging or gas infall, and only treats stellar mass loss in an instantaneous manner (see Springel & Hernquist 2003).

to guarantee similar noise properties. We randomized the sub-pixel position of the simulated galaxies, but find that the recovered structural properties are independent of this treatment.

In the following, we first analyze the *true* half-mass (§3) and half-light (§5) radii of the simulated galaxies as measured from the full (noise-free and high-resolution) information available from simulation and radiative transfer. Next, we include the effects of pixelization, finite resolution, and limited signal-to-noise by running the two-dimensional fitting code GALFIT (Peng et al. 2002) on the real and mock NIC2 images (§6).

### 3. SIMULATED MERGER REMNANTS ON THE SIZE - MASS RELATION

Wuyts et al. (2009b) demonstrated that the integrated stellar population properties (rest-frame optical and optical-to-NIR colors, as well as specific star formation rates) of simulated merger remnants are consistent with those of observed quiescent galaxies at  $z \sim 2$ . Here, we investigate whether a major merger formation scenario can also account for the remarkable compactness of the observed quiescent systems. A useful diagnostic to address this question is the size-mass relation. In Figure 3, we mark the local spheroid size-mass relation (Shen et al. 2003) with a solid line. As reliable size measurements of complete samples of high-redshift quiescent galaxies are only available over a narrow mass range, we indicate a fiducial size-mass relation at redshift  $z \sim 2.3$  (dashed line) by assuming the  $z \sim 0$  slope and adopting the median size and mass of the vD08 sample as zero-point anchor. We note that both observational (Trujillo et al. 2006; Ryan et al. 2010) and theoretical (Khochfar & Silk 2006a) studies have suggested that the size-mass relation becomes shallower with redshift. Ryan et al. (2010) report a mass dependence of the power-law index  $\alpha$  in the size evolution  $R_e/R_{e,z=0} = (1+z)^{-\alpha}$  of  $\alpha \approx -1.8 + 1.4 \log(M_*/10^9 M_\odot)$ . We caution that this fit is driven by measurements of galaxies at  $0 < z < 2$ , and, as stated by Ryan et al. (2010), should be considered preliminary at best. Nevertheless, it is illustrative to plot the corresponding size-mass relation at  $z \sim 2.3$  (dotted line). We conclude that the ultra-compactness of massive ( $> 10^{11} M_\odot$ ) quiescent galaxies at  $z \sim 2$  is a robust result. Tighter constraints on the sizes of high-redshift spheroids of lower mass will be essential to understand whether they formed through similar mechanisms. The main focus of this paper is on compact galaxies at the high-mass end.

Overplotted in Figure 3, we show the 2D (i.e., projected) half-mass radii of simulated merger remnants as a function of their stellar mass, as seen from 100 viewing angles uniformly spread over a sphere. We consider merger simulations with a range of stellar masses, and in each case only plot the snapshots more than 100 Myr after the final starburst. Encircled are the remnants produced by merging progenitors that were scaled to represent  $z = 3$  disks (i.e., reaching the remnant phase around  $z \sim 2.3$ ). The other simulations started out with progenitors scaled to represent local disk galaxies. For every simulation, we define a dissipational fraction  $f_{\text{gas}}$  as the gas fraction of the system 125 Myr before the peak in star formation rate (SFR) is reached. Even though some of our simulations start with initial gas fractions as high as

80%,  $f_{\text{gas}}$  rarely reaches values above 50%, because rapid star formation in the progenitor disks, especially during first passage, consumes significant amounts of gas before final coalescence.

Figure 3 clearly illustrates that, at a given mass, the size of a merger remnant is smaller when the dissipational fraction is higher, and even more so when the progenitor disks had a more compact nature to start with. Tidal torques are responsible for channeling large amounts of gas to the central region (Barnes & Hernquist 1991, 1996) where it is consumed in a starburst (Mihos & Hernquist 1994, 1996). We conclude that the location of the observed  $z \sim 2$  quiescent galaxies on the size-mass diagram (the vD08 sample has median properties  $r_e = 0.9$  kpc,  $M = 1.7 \times 10^{11} M_\odot$ ) can straightforwardly be explained by major merger activity provided the progenitors at high redshift were more gas-rich and had scale-lengths smaller than today's disk galaxies. This idea was first formulated by Khochfar & Silk (2006a), and is further detailed by Hopkins et al. (2009a; 2010a). Significant observational support for increased gas fractions in star-forming galaxies towards higher redshift was inferred from H $\alpha$  spectroscopy by Erb et al. (2006), and more recently confirmed on the basis of molecular line measurements (Baker et al. 2004; Coppin et al. 2007; Daddi et al. 2008; Tacconi et al. 2010). Likewise, a decrease in the size of star-forming galaxies at a given mass is observationally well established (Trujillo et al. 2006; Franx et al. 2008; Williams et al. 2010).

### 4. KINEMATICS

A proper characterization of galaxy structure requires knowledge of the mass-to-light ratio to determine the stellar mass, and of its gradient to translate the measured half-light radius to a radius containing half the mass (see §5). One way to circumvent  $M/L$  ratio effects, is probing the central potential directly through kinematics. However, measuring the velocity dispersions of quiescent  $z \sim 2$  galaxies from their absorption line spectra is extremely expensive in terms of telescope time. To date, one such measurement (van Dokkum, Kriek & Franx 2009) at  $z > 2$  has been carried out, totaling 29 hours on a 8m class telescope. At somewhat lower redshift and mass ( $\log M = 10 - 11$ ), a stacked measurement of similar red nuggets at  $1.6 < z < 2.0$ , as well as two individual measurements at  $z \sim 1.4$  were presented by Cappellari et al. (2009). In Figure 4, we compare the measured velocity dispersion to the virial estimator  $\sqrt{\frac{M}{r_e}}$ , where  $M$  is the stellar mass derived from SED modeling. The dashed line indicates the proportionality followed by present-day early-type galaxies (van Dokkum & Stanford 2003; Cappellari et al. 2006). Color-coded by their gas fraction shortly before the final starburst, we overplot the same simulated merger remnants whose progenitors were scaled to represent high-redshift star-forming galaxies as displayed in Figure 3. Both the observed and simulated quiescent galaxies show a clear correlation between the measured velocity dispersion and what would be estimated based on virial arguments. Within the error bars, the observational results are all consistent with having the same scaling between  $\sqrt{\frac{M}{r_e}}$  and  $\sigma$  as early-type galaxies in the nearby universe. Simulations of gas-rich merg-

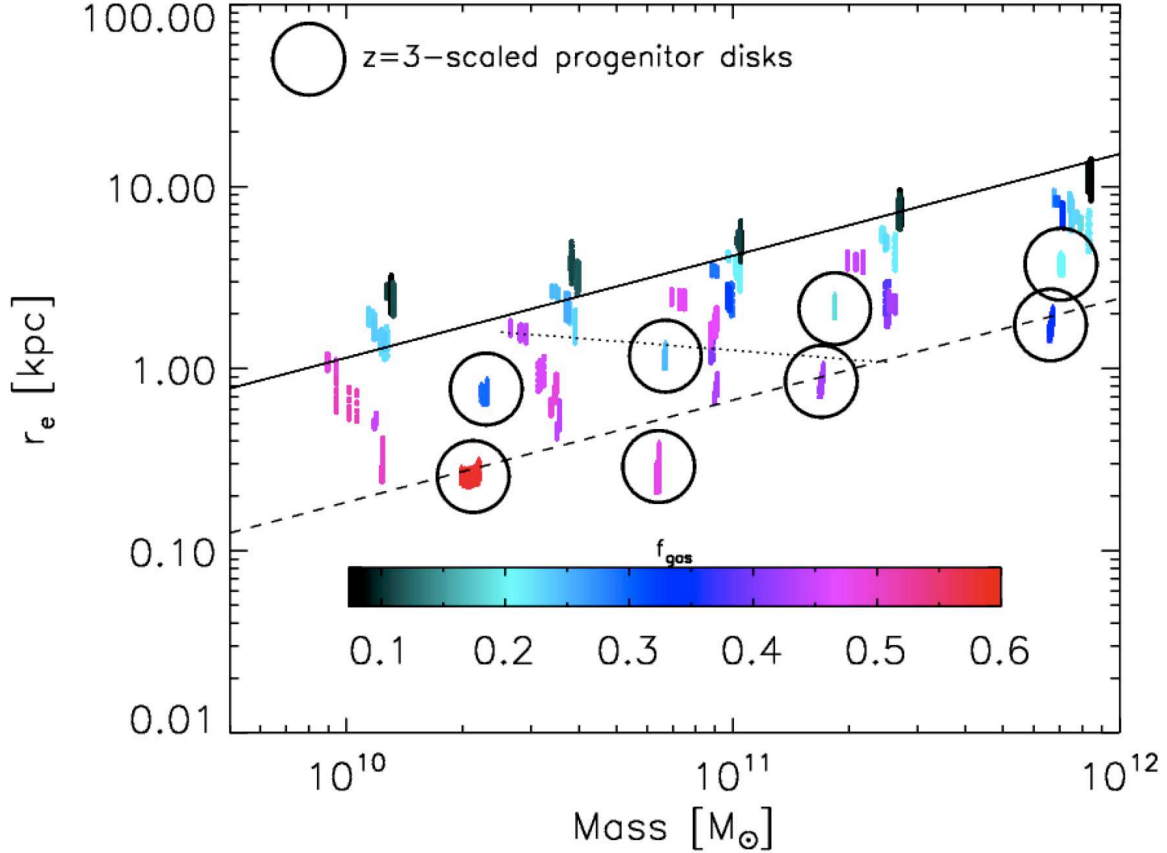


FIG. 3.— Size-mass diagram of simulated merger remnants, color-coded by the gas fraction of the merger from which they descend, measured 125 Myr prior to the peak in star formation rate. Simulations where the progenitors were scaled to represent disk galaxies at  $z = 3$  are encircled. The solid line indicates the size-mass relation of present-day early-type galaxies (Shen et al. 2003). The quiescent galaxies at  $z \sim 2.3$  from vD08 lie on the dashed line. The dotted line indicates the size-mass relation at  $z \sim 2.3$  based on an extrapolation of the mass-dependent size evolution measured by Ryan et al. 2010. At a given mass, merger remnants are more compact as the dissipational fraction increases.

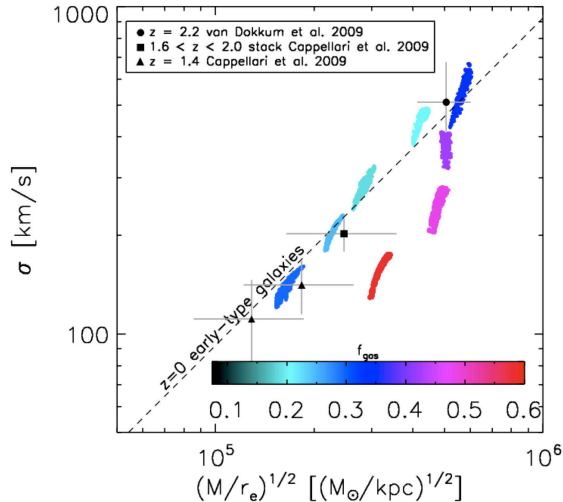


FIG. 4.— Velocity dispersion of quiescent galaxies at  $1.4 < z < 2.2$  as function of the virial estimator  $\sqrt{M/r_e}$  based on their stellar mass and size. Simulated merger remnants span a similar range, but at a given  $\sigma$  extend to higher values of the virial estimator when the dissipational fraction is large ( $> 40\%$ ).

ers are able to produce remnants with similar velocity dispersions. At a given velocity dispersion, the virial es-

timator  $\sqrt{M/r_e}$  is larger for runs with a higher dissipational fraction, implying that mergers of varying dissipational fraction are non-homologous (see also Robertson et al. 2006; Hopkins, Cox & Hernquist 2008). Briefly, the scaling factor  $k$  in the relation

$$\sigma = k \sqrt{\frac{M}{r_e}}, \quad (4)$$

where  $M$  is the stellar mass and  $r_e$  the stellar half-mass radius, depends on the profile shape of the stellar mass distribution (lower  $k$  for cuspy systems), and on the baryon-to-dark matter ratio within the stellar effective radius (lower  $k$  for more baryon-dominated centers). Our simulations show that both factors are a strong function of the dissipational fraction  $f_{\text{gas}}$  of the merger. Systems with larger  $f_{\text{gas}}$  are increasingly baryon-dominated in their centers. Their cuspy profile shapes are discussed at length in Section 6.1.

Although such measurements are not yet available observationally at  $z \sim 2$ , it is interesting to consider the degree of rotation expected in high-redshift compact quiescent galaxies. To this end, we study the ratio of rotational over random motion ( $v_{\text{maj}}/\sigma$ , where the rotation velocity is measured along the major axis) as a function of ellipticity in Figure 5. The gray-coded distribution indicates the locus occupied by quiescent merger remnants



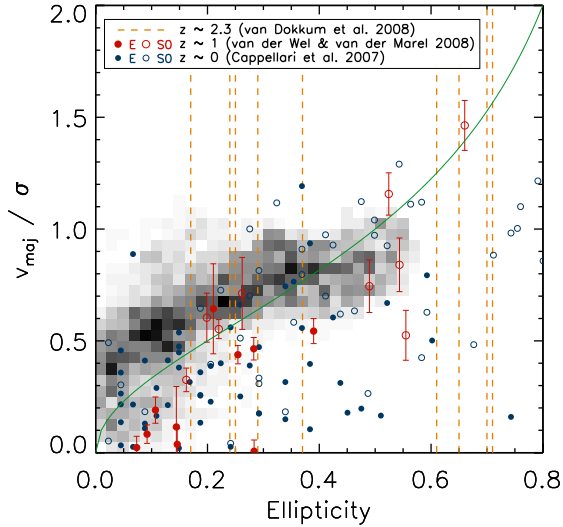


FIG. 5.—  $(v/\sigma, \epsilon)$  diagram for simulated merger remnants of  $\sim 10^{11} M_{\odot}$  and  $\sim 1$  kpc size (gray-coded distribution). Ellipticities of quiescent galaxies at  $z \sim 2.3$  with similar mass and size from vD08 are indicated with dashed vertical lines. Early-type galaxies at  $z \sim 0$  and  $z \sim 1$  are overplotted for reference. The green line marks the relation expected for an oblate isotropic rotator. The simulations suggest that rotation may on average play a more dominant role in early-type galaxies at high redshift than at low redshift, due to the increasingly dissipational processes through which they formed.

that match the vD08 galaxies in size and mass. These remnants are the product of gas-rich merger simulations with a range of orbital configurations, and we observe them from 100 sightlines uniformly distributed over a sphere. The green line marks the relation expected for an oblate isotropic rotator (Binney 1978):

$$\frac{v}{\sigma} = \sqrt{\frac{\epsilon}{1 - \epsilon}} \quad (5)$$

Vertical dashed lines indicate the ellipticities of the  $z \sim 2.3$  compact galaxies of vD08, as measured on the high-resolution NIC2 images. For reference, we also plot the location of massive early-type galaxies (of larger size than those at  $z \sim 2$ ) at  $z \sim 1$  (van der Wel & van der Marel 2008) and at  $z \sim 0$  (a complete sample extracted from the HyperLeda database by Paturel et al. 2003, as detailed by van der Wel & van der Marel 2008). The closed and open circles represent galaxies with an E and S0 morphology respectively.

The rotation parameter of the simulated merger remnants increases with ellipticity. At a given ellipticity, the compact remnants show a larger degree of rotational support than the bulk of early-type galaxies today. Their kinematics resemble those of the fastest rotators of the  $z \sim 0$  sample at each ellipticity. Cox et al. (2006) demonstrated that the rotation parameters and flattening of local spheroids with less rotation can be reproduced by merger simulations tuned to lower redshift, with lower gas fractions (see also Naab, Jesseit & Burkert 2006). A hint of increasing rotational support towards higher redshifts, where mergers are expected to be increasingly dissipational, may already be observed when comparing the measurements at  $z \sim 1$  to those at  $z \sim 0$ . It remains to be seen whether this trend extends to  $z \sim 2$ ,

and whether similarly high values of  $\frac{v}{\sigma}$ , of up to unity, are present as anticipated by our simulations. The large range of ellipticities in the vD08 sample, reaching values of  $\epsilon > 0.6$  which are larger than found in our simulations, may point to rotation being indeed important in these systems.

## 5. $M/L$ RATIO GRADIENTS

Size measurements have traditionally been carried out using one waveband only, typically the longest wavelength available at high resolution. By definition, this technique probes a monochromatic surface brightness profile. Evidently, the half-light radius derived from it equals the physically more meaningful half-mass radius only under the assumption of a spatially constant  $M/L$  ratio.

Having established that gas-rich mergers are a viable mechanism to collect  $\sim 10^{11} M_{\odot}$  of baryonic material in a  $\sim 1$  kpc radius, we now use our simulations to test this assumption for the quiescent remnants. Using the radiative transfer methods described in §2.2, we compute the half-light radius in three rest-frame wavebands  $U$ ,  $V$ , and  $J$ , and contrast it with the half-mass radius of the system for 100 lines of sight. Figures 6 and 7 show the resulting light-to-mass size ratio  $r_{e,\text{light}}/r_{e,\text{mass}}$  as a function of time since the merger for the same simulation shown in Figure 2(c). The central line indicates the median evolution over all viewing angles, whereas the light and dark shaded regions mark the central 50% and 100% percentiles respectively.

Panels on the left illustrate the time evolution of  $r_{e,\text{light}}/r_{e,\text{mass}}$  ignoring attenuation by dust. In this case, all scatter at a given time is due to projection effects. The scatter is limited to a few percent in rest-frame  $V$ , which is the band most closely corresponding to F160W at  $z \sim 2.3$ . Initially, as many new stars are formed in the nuclear starburst, the intrinsic light profile is more centrally concentrated than the stellar mass profile (i.e.,  $r_{e,\text{light}}/r_{e,\text{mass}} \ll 1$ ). On timescales of a few hundred Myr, as the bright and short-lived O and B stars die out, the nuclear emission dims with respect to the outer parts of the galaxy, and the  $M/L$  gradient flattens. In fact, around 400 Myr after the peak in star formation rate, the light profile in the rest-frame optical becomes more extended than the mass profile. This trend is more pronounced as we consider shorter wavelengths, reaching  $r_{e,\text{light}}/r_{e,\text{mass}} \sim 2$  in rest-frame  $U$ . The reason for this reversed  $M/L$  gradient is that the young stars in the center formed out of more metal-enriched gas than the stars that constitute most of the galaxy outskirts, making them fainter and cooler (Binney & Merrifield 1998, and references therein). We illustrate the physical conditions underlying the  $M/L$  ratio gradients in Figure 8 for the snapshot 480 Myr after the merger. At this time, the remnant has a specific star formation rate ( $3.7 \times 10^{-11} \text{ yr}^{-1}$ ) and broad-band colors similar to those of observed quiescent galaxies. Plotting stellar age as function of distance from the stellar particles to the center (Figure 8a), three loci in age can be distinguished, corresponding to stars formed in the progenitor disks, during first passage, and during final coalescence. The radial position in the merger remnant is clearly correlated with the epoch at which the stars were formed. Figure 8a also illustrates that the low level trickle of star formation

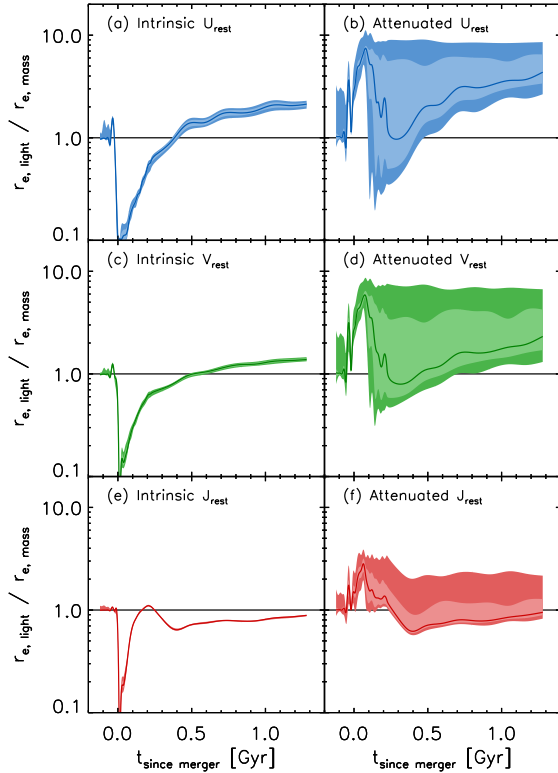


FIG. 6.— Ratio of half-light to half-mass radius as function of time since the merger, as determined from the intrinsic (unattenuated) photometry (*left panels*) and the attenuated photometry (*right panels*). Mass-to-light ratio gradients originate due to a combination of age, metallicity, and extinction gradients that depend on time, wavelength, and viewing angle. The half-light radius of quiescent merger remnants measured in the rest-frame  $V$ -band is typically larger by a factor 1.5 to 2 than the projected radius containing half the mass. This ratio increases to a factor 2-3 in the rest-frame  $U$ -band. Our result implies that the observed compact quiescent galaxies (see, e.g., vD08), if formed by a similar gas-rich merger process, may be even more compact in terms of mass than previously assumed.

present after the nuclear starburst happens mostly outside the stellar half-mass radius ( $r_{e,3D} = 0.9$  kpc). This is a secondary effect contributing to the larger extent of the light profile compared to the mass profile. Figure 8b demonstrates the presence of a negative stellar metallicity gradient, of slope  $\frac{\Delta \log(Z)}{\Delta \log(r/r_e)} = -0.35$ . This slope is a factor 1.5 to 2.5 steeper than that of typical massive early-type galaxies today (Rawle, Smith & Lucey 2010; Kuntschner et al. 2010), although those exhibit a large scatter in gradients. Together with their compact nature (§3) and fast rotation (§4), this implies the gas-rich merger remnants at  $z \sim 2$  cannot evolve passively into present-day massive ellipticals. Subsequent (dry) merging has been proposed as a mechanism to slow the rotation, grow the size, and dilute the metallicity gradient, with the extent of the dilution dependent on the properties of the merger (Di Matteo et al. 2009).

In addition to stellar age and metallicity, the gas and dust distribution and extinction column towards stellar particles also vary radially. The remaining gas in the  $1 < r < 30$  kpc range has a negative metallicity gradient

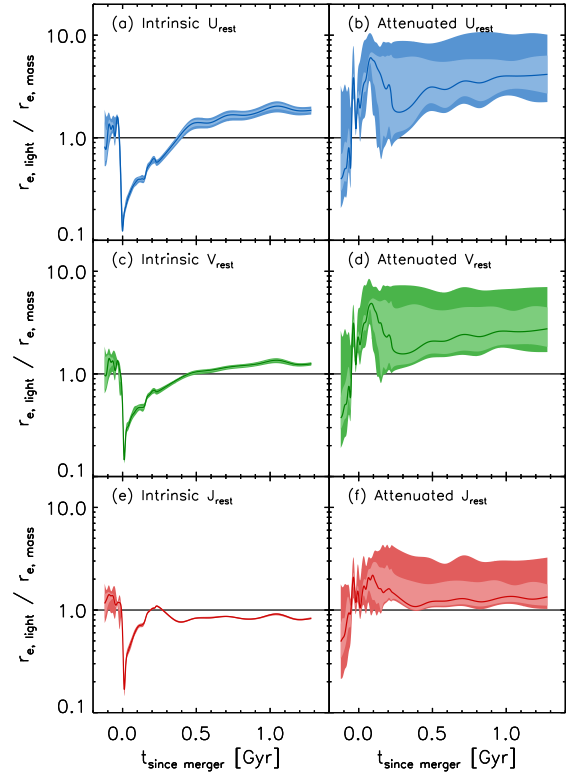


FIG. 7.— Idem as Figure 6, but with photometry computed with the SUNRISE radiative transfer code.

(Figure 8c), while at even larger radii the SPH gas particles show a wide spread in metallicities. The normalized cumulative distribution of dust (taken to be proportional to the metallicity-weighted gas distribution) is contrasted with that of stars and gas in Figure 8d. The corresponding spherically averaged density profiles, normalized to the density at 1 kpc, are presented in Figure 8e. The gas is distributed over scales that are an order of magnitude larger than that of the stellar distribution. Both gas and dust ( $\sim$  metallicity-weighted gas) reach a peak density near the stellar half-mass radius ( $r_{e,3D} = 0.9$  kpc). The tail of young stars at  $\sim 1$  kpc visible in Figure 8a shows that it is also here that the small amount of star formation that is still present after the merger ( $\frac{SFR}{M} = 3.7 \times 10^{-11} \text{ yr}^{-1}$ ) takes place. Gas that during earlier phases resided within this radius has largely been consumed by star formation, or has been blown out by feedback processes from supernovae and AGN. Although this is not visible in the spherically averaged density profile of Figure 8d, the central cavity devoid of gas and dust is not spherically symmetric, but rather axisymmetric. The resulting radial distribution of optical depths towards the stellar particles therefore depends on the line of sight. We illustrate this distribution for two characteristic viewing angles in panel (f) and (g). For the viewing angle presented in panel (f), the effective attenuation of the region within the half-mass radius is larger than that outside. Consequently, the attenuated  $V$ -band half-light radius viewed from this angle is 4.8 times larger than the half-mass radius. For the viewing angle of panel (g), the opposite is the case and the resulting attenuated  $V$ -band half-light radius is smaller than the half-mass



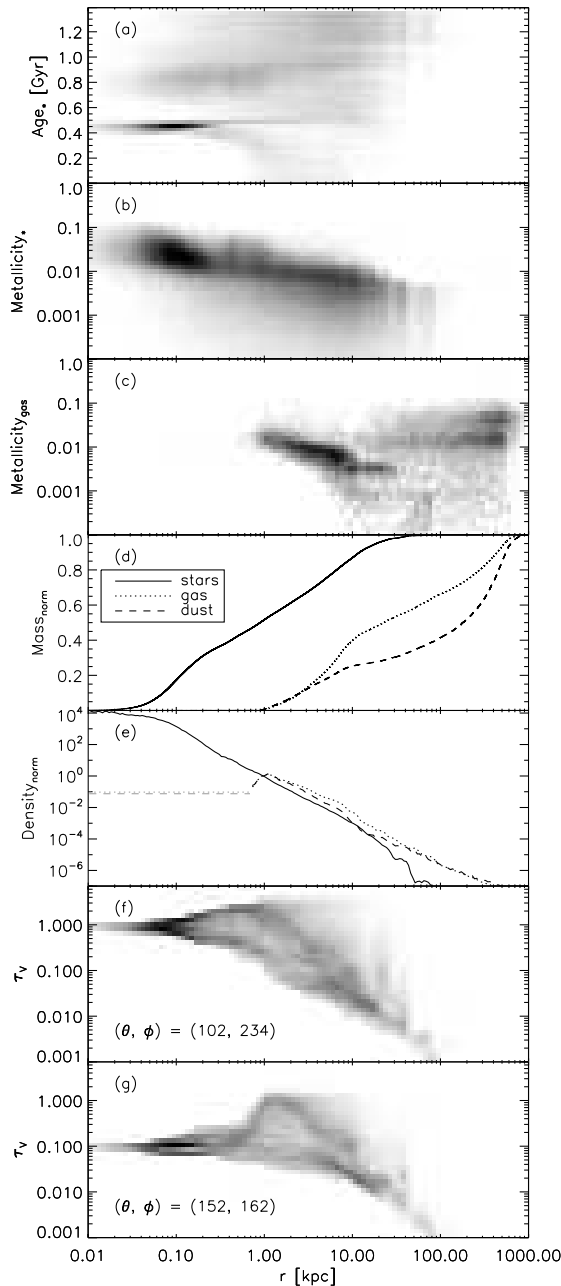


FIG. 8.— Radial stellar population profiles of a merger simulation snapshot during the spheroid phase, half a gigayear after final coalescence. We show (a) the distribution of stellar age as a function of distance to the galaxy center, (b) the stellar metallicity increasing towards the center, (c) the radial dependence of the gas-phase metallicity, (d) the normalized stellar, gas and dust mass distributions, (e) their respective density profiles normalized to the density at  $r = 1$  kpc, (f) and (g) the distribution of optical depths towards all stellar particles for two random viewing angles.

radius by a factor 1.4.

The right-hand panels of Figure 6 illustrate how the superposition of a dust, age, and metallicity gradient translates into the light-to-mass size ratio  $r_{e,\text{light}}/r_{e,\text{mass}}$ , and how this quantity depends on time relative to the merger, line of sight, and wavelength. During the nuclear starburst, the  $M/L$  ratio gradient is completely

reversed with respect to the intrinsic (unattenuated)  $M/L$  ratio gradient, because of central dust obscuration. The median light-to-mass size ratio then drops, reaching  $r_{e,\text{light}}/r_{e,\text{mass}}$  values below 1 around 300 Myr after the peak in star formation rate, as the central dust content decreases while the young, massive stars in the center are still alive. Finally, as the system reaches a quiescent remnant phase ( $t_{\text{since}} \gtrsim 500$  Myr), the age gradient has faded and the combination of a negative extinction and metallicity gradient results in typical half-light radii of  $2.0^{+2.9}_{-0.6}$ ,  $1.1^{+2.1}_{-0.2}$ , and  $0.7^{+0.3}_{-0.0}$  times the half-mass radius at  $t_{\text{since}} = 500$  Myr in rest-frame  $U$ ,  $V$ , and  $J$  respectively. At  $t_{\text{since}} = 1$  Gyr, the half-light radii in the rest-frame  $U$ -,  $V$ -, and  $J$ -band are  $3.4^{+2.0}_{-0.6}$ ,  $1.8^{+1.9}_{-0.3}$ , and  $0.8^{+0.3}_{-0.0}$  times the half-mass radius. Here, the error bar indicate the central 50% percentile of the scatter due to line-of-sight variations. Typically, the distribution shows an extended tail towards large  $r_{e,\text{light}}/r_{e,\text{mass}}$  ratios. Both the line-of-sight scatter and the median value of  $r_{e,\text{light}}/r_{e,\text{mass}}$  increase towards shorter wavelengths.

Computing the synthetic photometry with the independent radiative transfer code SUNRISE (Figure 7) gives results that are qualitatively consistent with those obtained from the LOS code. SUNRISE predicts typical light-to-mass size ratios of 3.6, 2.4, and 1.3 in rest-frame  $U$ ,  $V$ , and  $J$  respectively during the quiescent phase. The sightline dependence shows a similar behavior as seen in the results from the LOS code, i.e., with a tail towards large  $r_{e,\text{light}}/r_{e,\text{mass}}$  ratios (ratios of 5 and above).

We tested the dependence of our results on the adopted attenuation law, on the assumed age and metallicity of stars present at the start of the simulation, and whether an age and/or metallicity gradient was already in place in the initial progenitor disks, and find consistent results with variations much smaller than those from sightline to sightline. Likewise, similar results were obtained from simulations where the progenitor disks were merged with a different orbital configuration.

Peirani et al. (2010) simulate minor mergers between an elliptical galaxy and a satellite (spiral galaxy), and find qualitatively similar stellar age gradients: the young stars that formed by dissipational processes reside in the center of the remnant. The evolution of half-light radii presented by Peirani et al. (2010) resembles that seen in intrinsic light in our major merger simulations. However, the dust columns, and therefore the impact of attenuation on the observed  $M/L$  gradients, are larger for the major than for the minor merger simulations. The assumption of a fixed dust-to-gas rather than dust-to-metal ratio, and the absence of AGN feedback in the Peirani et al. (2010) simulations may also contribute to differences in the predicted  $M/L$  gradients.

In summary, we find that the interplay between an age, metallicity, and dust gradient manifests itself as a  $M/L$  ratio gradient that depends on time, line of sight and wavelength. Since an observer can only probe the latter parameter directly, the detection of color gradients showing preferentially red cores in compact quiescent galaxies would support the presented scenario. Moreover, from the simulations we expect the internal color gradients to be correlated with the integrated rest-frame optical color (see Figure 9). We stress that the presence of a red core does not necessarily imply inside-out growth. In fact, in this scenario, and in the absence of subsequent merging

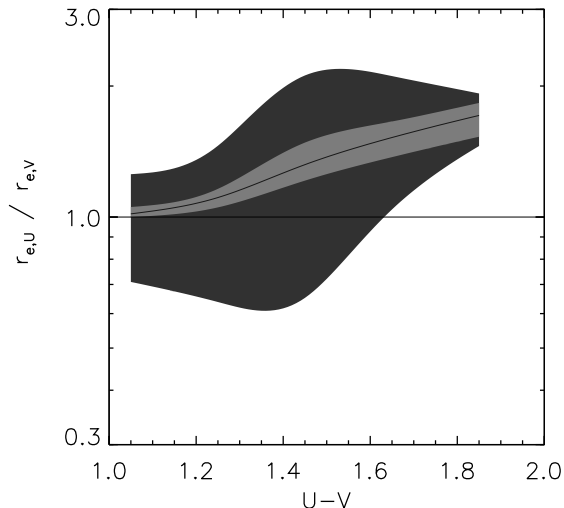


FIG. 9.— Ratio of  $U_{\text{rest}}$  to  $V_{\text{rest}}$  half-light radius as function of integrated color. The central line indicates the median relation, whereas the light- and dark-gray polygon indicate the 50% and 100% percentiles of distribution over 100 lines-of-sight uniformly spread over a sphere.

(see §6.3), the bulk of the youngest stars resides in the center, but the effect of the age gradient on the internal color profile is compensated by the presence of metallicity and extinction gradients. Finally, if negative  $M/L$  ratio gradients are indeed present, our results may imply that the observed quiescent galaxies may be an order of magnitude ( $\sim 2^3$ ) more dense than previously inferred from HST/NICMOS observations (vD08).

## 6. SURFACE BRIGHTNESS PROFILES

### 6.1. The cuspieness of simulated merger remnants

We established that gas-rich mergers are a viable mechanism to assemble dense stellar systems of  $\sim 10^{11} M_{\odot}$  and  $\sim 1$  kpc size (§3), and that such a scenario would leave a color and  $M/L$  ratio gradient as imprint (§5). Now, we go beyond the zeroth-order structural measurement of size and compare how the surface brightness profiles of simulated merger remnants compare to those of observed quiescent galaxies at  $z \sim 2$ .

For this purpose, we use the mock F160W observations described in §2.3 that are matched in terms of PSF, pixel size, wavelength, redshift, and noise properties to the NIC2 observations of high-redshift spheroids by vD08. We analyze the real and mock observations in concert with the two-dimensional fitting code GALFIT (Peng et al. 2002) using identical settings. In Figure 10, we show postage stamps of the real NIC2 images by vD08. Next to each image, we plot the residual images after subtracting the best-fit Sersic profile when leaving the Sersic index  $n$  free, or fixing it to  $n = 2$ ,  $n = 3$ ,  $n = 4$ , and  $n = 10$  respectively. We rank the objects by best-fit Sersic index and find they span a large range from  $n = 4.5$  to  $n = 0.5$ , reproducing the vD08 results. In most cases, fixing the Sersic index to  $n = 10$  leads to significantly larger residuals than leaving  $n$  free.

Repeating the analysis for random viewing angles of a simulated merger remnant (Figure 11), we obtain strikingly different results. For the majority of sightlines, we find that exponential ( $n = 1$ ) and even de Vaucouleurs

( $n = 4$ ) profiles provide a poor fit to the mock data. Their  $n_{\text{fix}} = 2 - 4$  residual images (illustrated in the top 6 rows of Figure 11) are characterized by a central positive peak, surrounded by a negative ring, outside of which a positive wing is barely visible above the noise. Our results remain unchanged when running GALFIT with the sky level left as a free parameter. The origin of this characteristic pattern becomes clear when considering a one-dimensional representation of the surface brightness, free of the PSF, noise, and pixelization effects of the mock observations (Figure 12a). Here, the black solid line indicates the median surface brightness profile of 100 sightlines uniformly distributed over a sphere. The dashed and dotted gray lines decompose the light into that of stars formed prior and during final coalescence respectively. As discussed extensively by Hopkins et al. (2008b; 2009b), the young component produces a central cusp, and the combination of the young and old component yields a profile that is poorly characterized by a simple Sersic index. The colored curves in Figure 12(a) illustrate Sersic profiles with a total luminosity and half-light radius identical to that of the simulated merger remnant. The radially alternating positive-negative-positive residual pattern is immediately apparent, as is the tendency to fit high values of  $n$ . It is important to note that this tendency is driven both by the presence of a central cusp (the amplitude of which depends on the amount of gas present at final coalescence) and by the presence of the strong wings to the profile (the amplitude of which is determined by the amount of gas consumed during the progenitor phase).

For a smaller number of sightlines (illustrated by the bottom 3 panels of Figure 11) a flat residual image is obtained when fitting a Sersic index in the range  $2 < n < 5$ . Obscuration of the central young component by dust is responsible for this sightline-dependent effect.

We demonstrate our findings with more statistical robustness (more lines of sight and timesteps, and simulations with different orbital configurations) in Figure 12(b). Here, we plot the profile shape (characterized by the best-fit Sersic index) as function of the half-light radius recovered by GALFIT. Large black circles are the vD08 compact galaxies. They have a median  $n = 2.3$ , well below the  $n = 4$  de Vaucouleurs profile that is characteristic for nearby spheroids. van Dokkum et al. (2010) attribute this evolution to minor merging building up the wings of the high-redshift compact nuggets over cosmic time. The Sersic profiles fitted to the simulated merger remnants (red dots) are significantly cuspier (higher  $n$ , adopting an upper bound of  $n = 10$ ). For the subset (about one fifth) of sightlines where the central cusp is sufficiently obscured by dust, the inferred half-light radius is several kpc, inconsistent with the observed compact systems.

We draw a similar conclusion from a direct comparison of the surface brightness profiles of our simulated merger remnants to that of a massive compact quiescent galaxy at  $z = 1.91$  in the Hubble Ultra Deep Field (Szomoru et al. 2010, see Figure 13). Szomoru et al. (2010) derive the deconvolved profile of this galaxy from very deep Wide Field Camera 3 (WFC3) imaging using a novel technique that corrects the best-fit Sersic profile with the residual of the fit to the observed image. They find that the surface brightness profile is well approximated by an  $n = 3.7$

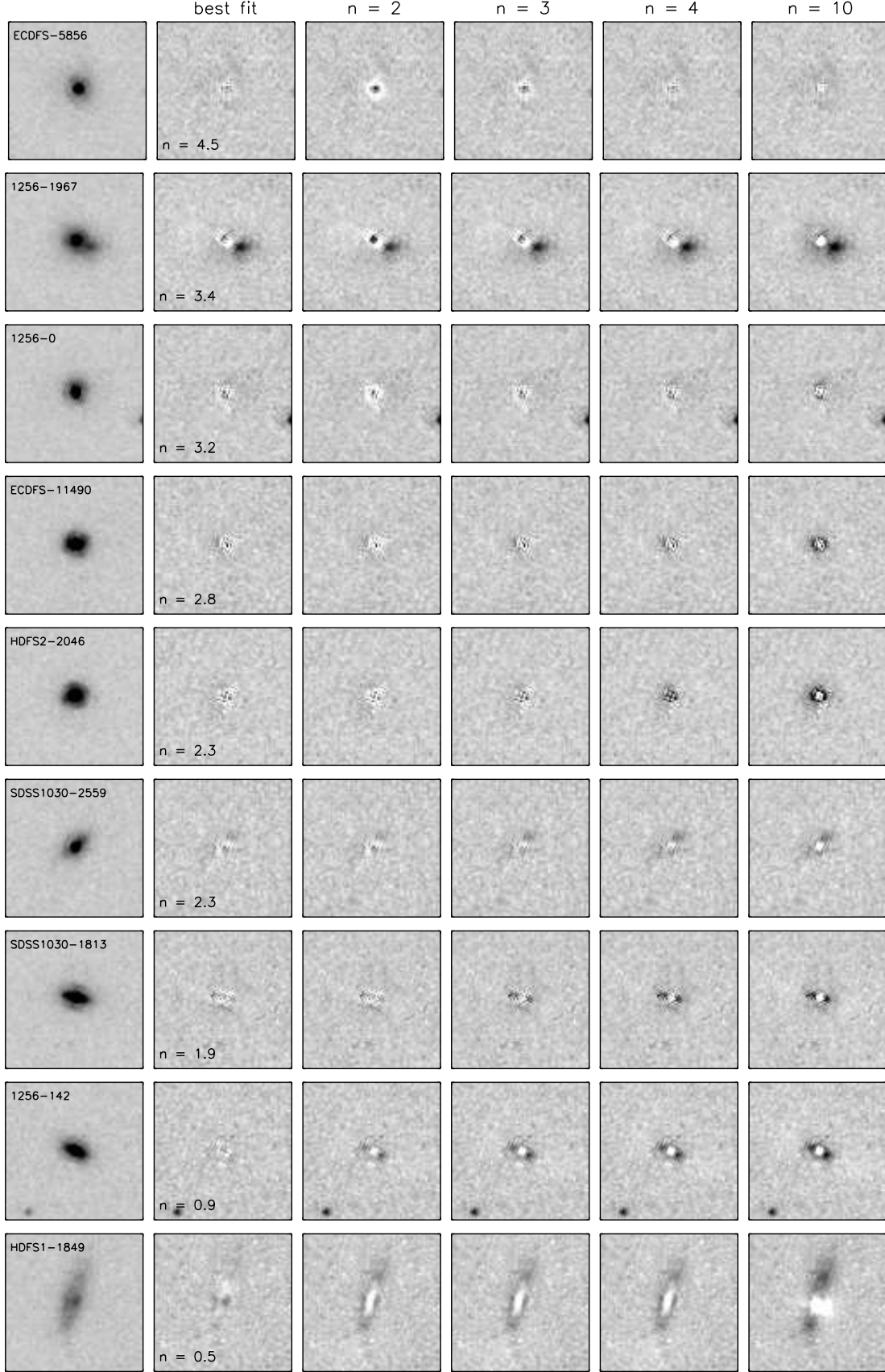


FIG. 10.— NIC2 F160W postage stamp images of the vD08 sample of quiescent galaxies, and residual images after subtracting the best fit when leaving  $n$  free, or fixing it to  $n = 2, 3, 4$ , and  $10$  respectively. The panels are sized  $3'' \times 3''$ , and for clarity the contrast of the residual images is double that of the observed image. Typically, the observed quiescent galaxies are best represented by Sersic profiles with  $n < 4$ .

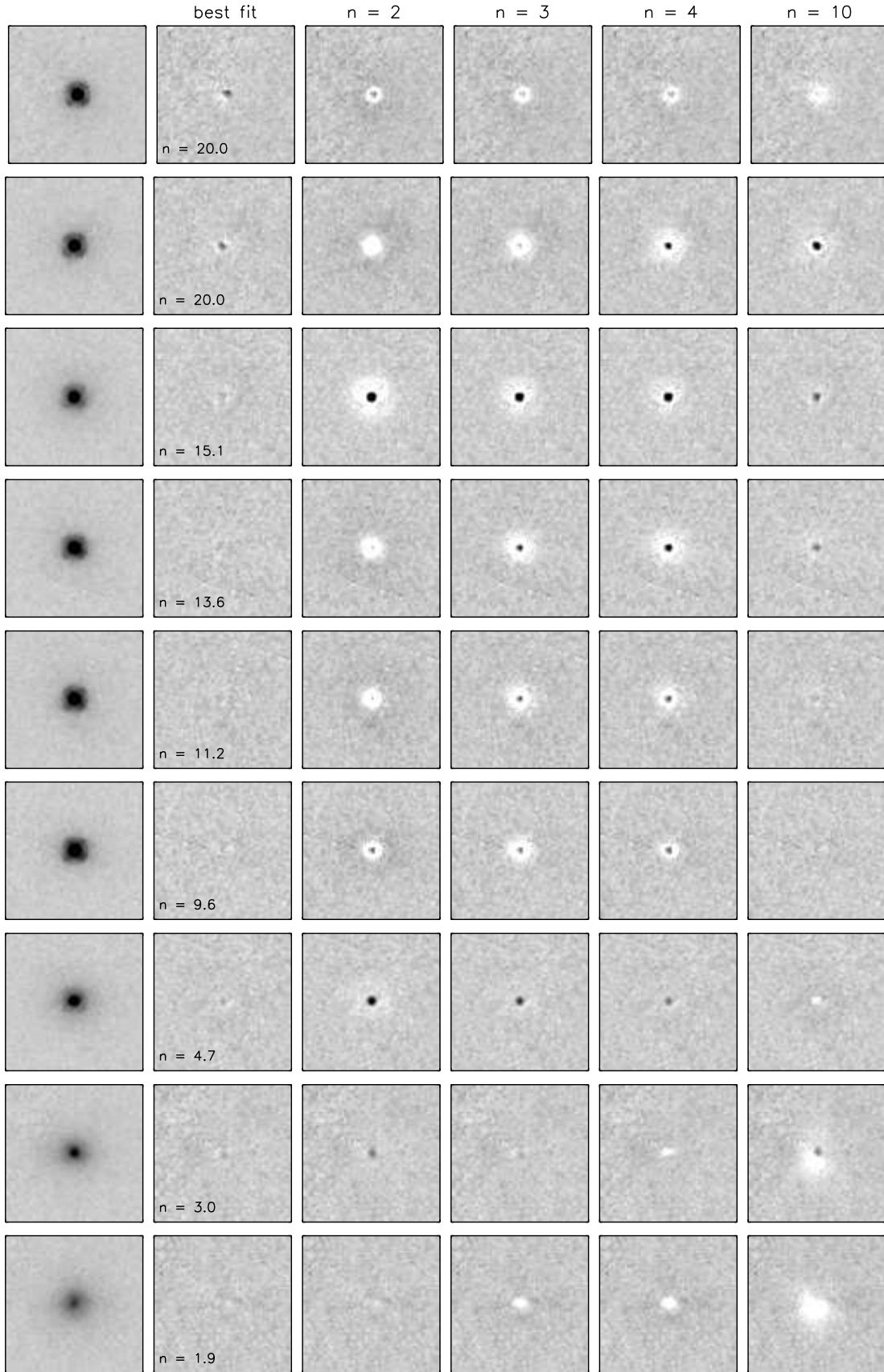


FIG. 11.— Mock NIC2 F160W observations of simulated merger remnants. The panels are  $3''$  on a side, corresponding to 24.6 kpc at  $z = 2.3$ . For 80% of the sightlines, the surface brightness profile is best fit by a cuspy profile (fit runs into the upper bound of  $n = 10$ ). Significant residuals remain when fixing the Sersic index to lower values. For about one fifth of the sightlines (illustrated in the bottom 3 rows) lower  $n$  are obtained, but the recovered half-light radius for these sightlines is larger than that of observed quiescent galaxies by a factor of  $\sim 5$ .

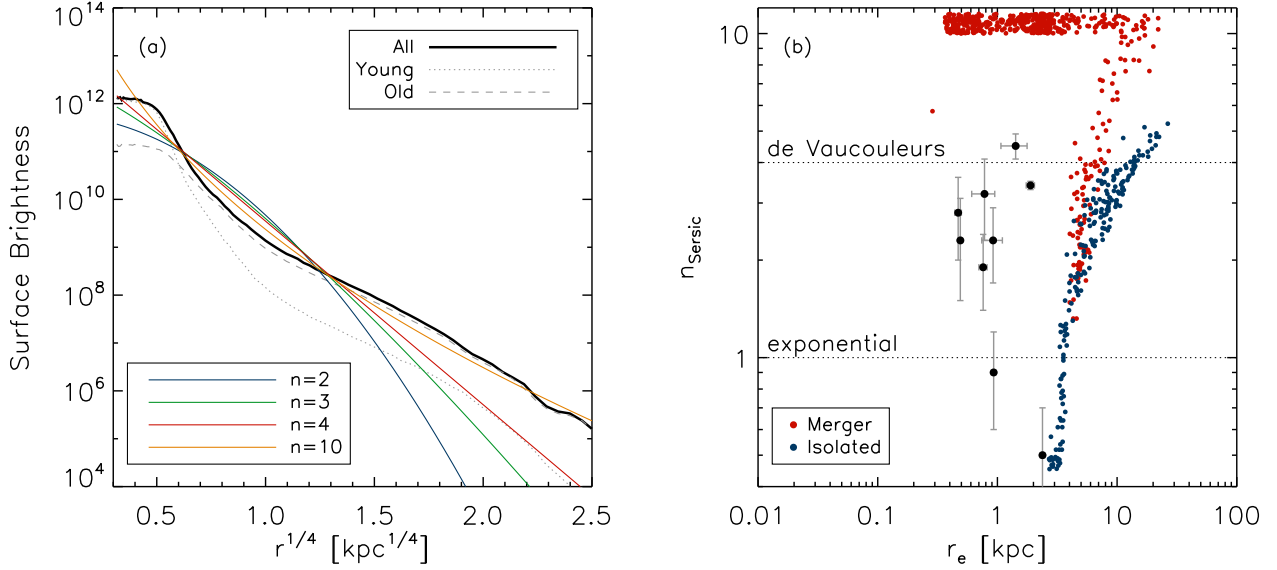


FIG. 12.— (a) Median rest-frame V-band surface brightness profile of a simulated merger remnant (black solid line), decomposed into a young (formed during the final burst, dotted gray line) and old (formed prior to final coalescence, dashed gray line) stellar component. In color, we overplot Sersic profiles of identical total luminosity and half-light radius for Sersic indices  $n = 2, 3, 4$ , and 10. The simulated merger remnant has a different nature than a pure Sersic profile, but is better approximated by a high value of  $n$  than a low  $n$ . (b) Sersic index as function of half-light radius as derived from GALFIT two-dimensional fitting, for the vD08 sample (large black symbols), and binary merger (red dots) and isolated disk (blue dots) simulations of similar mass placed at a similar redshift ( $z = 2.3$ ). Neither merger nor disk simulations simultaneously reproduce the size and profile shape of the observed quiescent galaxies.

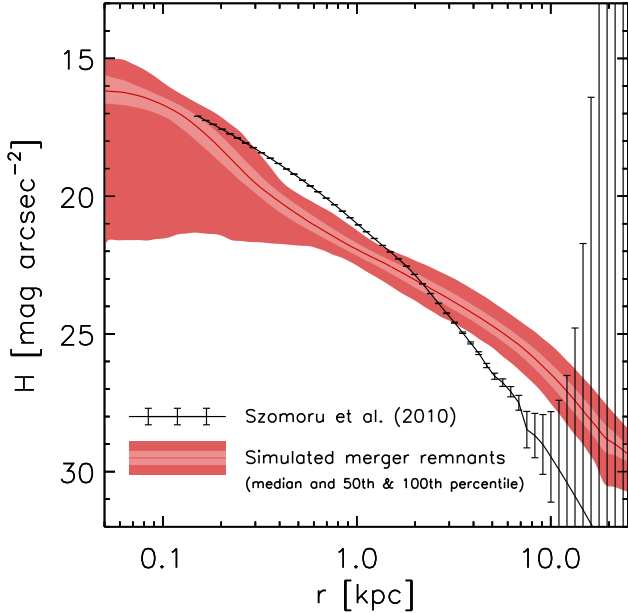


FIG. 13.— Direct comparison of the surface brightness profiles of simulated merger remnants with the deconvolved profile of a massive, compact galaxy at  $z = 1.91$  in the Hubble Ultra Deep Field (Szomoru et al. 2010). The profile of the observed quiescent galaxy falls off more rapidly at large radii than the simulated profiles.

Sersic profile. Typically, our simulated merger remnants have a higher surface brightness in the  $r > 2$  kpc wings relative to the surface brightness in the  $0.2 < r < 2$  kpc range.

The ability to correctly recover the true half-light radius known from the simulation depends on the upper bound set on the Sersic index. For  $n_{\text{max}} = 10$ , we find a systematic overestimate of the size by  $\sim 40\%$ , whereas

setting  $n_{\text{max}} = 4$  improves the size measurement to about  $\sim 10\%$  in the median, with a scatter in  $\frac{\Delta r_e}{r_e}$  of  $\sim 0.3$ . So, whereas the mock images for the majority of sightlines are best fit by high values of  $n$ , these best fits do not properly recover the true half-light radius of the system. This emphasizes the fact that an individual Sersic profile poorly describes its structure.

We assessed the impact of observational depth by artificially decreasing the signal-to-noise ratio of our mock observations (in practice, we reduce the source brightness, and add them to empty regions of the same NIC2 images). Running GALFIT with  $n_{\text{max}} = 10$ , this yields an increase in both the systematic size overestimate and the scatter in  $\frac{\Delta r_e}{r_e}$  over a range of viewing angles. Adopting  $n_{\text{max}} = 4$ , we find that, in the median, the recovered size is consistent with the true size over the full range of input source magnitudes  $21 < \text{mag}_{F160W} < 24$ . However, the scatter in  $\frac{\Delta r_e}{r_e}$  does increase by a factor 2-3 as we compare sources with  $\text{mag}_{F160W} = 24$  to sources of identical profile shape with  $\text{mag}_{F160W} = 21$ . We caution that different biases may be at play in the size measurement of observed compact quiescent galaxies such as the vD08 sample. Their intrinsic profile shape (i.e., noise-free and at infinite resolution) is unknown, but we did demonstrate it differs from that of our sample of simulated merger remnants as they translate into different (mock) observed properties. As an independent test, we also inserted pure Sersic profiles of  $\sim 1$  kpc size, with  $1 \leq n \leq 4$  and a range of luminosities into empty regions of the NICMOS images. Running GALFIT on them, we find qualitatively similar results regarding potential biases in size measurements. The scatter in the recovered size increases with decreasing signal-to-noise ratio. Whereas profiles of similar magnitude as the galaxies from vD08 ( $21 < \text{mag}_{F160W} < 22$ ) were recovered cor-



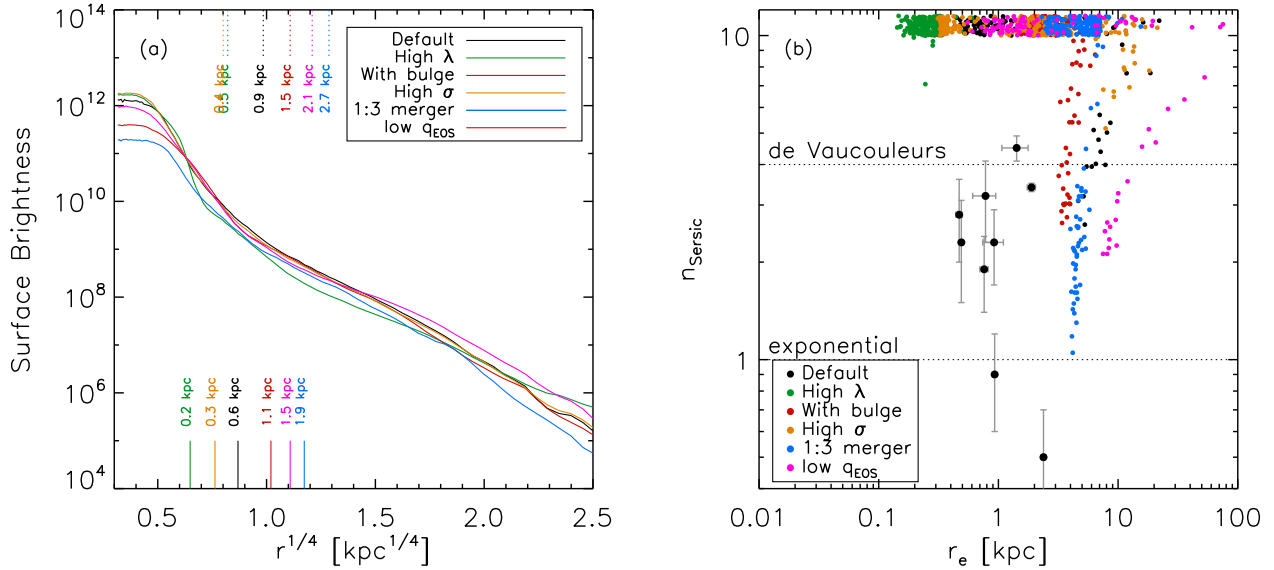


FIG. 14.— Idem as Figure 12, but for a series of simulations where the progenitor properties were varied. Vertical lines at the bottom of panel (a) indicate the half-light radii in the rest-frame V-band for which the surface brightness profiles are plotted. Dotted vertical lines on the top of panel (a) indicate the radii containing half of the rest-frame U-band light. When running GALFIT on mock NIC2 observations of the simulations placed at  $z \sim 2.3$ , the inferred Sersic index and size (b) span a different part of parameter space than covered by the vD08 sample of observed quiescent galaxies (*large black circles*).

rectly, systematic overestimates of the size by a factor 1.06 (1.2) in the median and 1.1 (2.2) in the mean are found when decreasing the brightness of non-exponential ( $2 \leq n \leq 4$ ) sources by 1 (2) magnitudes. In other words, perhaps counter-intuitively, size measurements from 2D surface brightness fitting on low signal-to-noise data may be biased towards size estimates that are too large, rather than too small.

Computing the mock observations of our simulated merger remnants using the LOS and SUNRISE radiative transfer codes yields qualitatively similar results. Namely, that the simulated surface brightness profiles tend to be cuspier, and in general occupy a different locus in  $(n, r_e)$ -space than the observed compact galaxies at  $z \sim 2$ . Moreover, we confirm that this difference is notable even given the limitations in depth and resolution of present-day observations. In detail, we note that, for a given simulation, the LOS code produces cuspier profiles than SUNRISE, yielding significant residuals after subtracting a  $n = 10$  fit (e.g., rows 1-3 of Figure 11) whereas these are mostly flat when running GALFIT on SUNRISE images (e.g., rows 4-6 of Figure 11).

Finally, we carried out a similar procedure on mock images of simulations where we let disk galaxies evolve in isolation. The initial disks are designed to have an exponential mass profile. We checked that GALFIT correctly recovers their  $n = 1$  profile shape from mock images of the first simulation snapshot (values of  $0.6 < n < 1$  are recovered for some sightlines due to dust obscuration in the central region). Eventually, since gas is consumed by star formation and we did not allow for gas replenishment, the simulated disk galaxies also reach low specific star formation rates. By the time this quiescent phase is reached, the disks have evolved in such a way that we find a range of Sersic indices similar to that of the vD08 sample (see Figure 12b). However, in all cases, their recovered size is a factor of several too large to reproduce the observed quiescent galaxies.

## 6.2. Dependence on progenitor properties

We now consider a few variations on the formation scenario for compact quiescent galaxies, with an emphasis on how they alter the consistency with observational constraints on size and profile shape. First, the apparent discrepancy in profile shape of the merger remnants may stem from inadequate assumptions on the structure of the progenitors from which they formed. Figure 14 presents a qualitative, but by no means complete, exploration of the vast parameter space in which progenitor properties can vary. First, we ran a simulation where the spin parameter of the dark matter halos was increased from  $\lambda = 0.033$  to  $\lambda = 0.1$  (*green*), with otherwise default settings. The higher spin parameter has a stabilizing effect on the gas disk, lowering the star formation rate during the progenitor phase, and increasing the gas fraction at the time of coalescence ( $f_{\text{gas}} = 0.64$  compared to  $f_{\text{gas}} = 0.42$  for our fiducial model). The result is an even more concentrated remnant. Less stars formed prior to the merger, but they were redistributed in such a manner that it is mainly at intermediate radii (around 1 kpc) that the surface brightness profile is devoid of light with respect to our default simulation. This is where the residual to a Sersic fit with  $2 < n < 4$  was already negative (see Figure 12a), causing the best fit to run into the upper bound set on  $n$  again. Second, we investigate a simulation with the same total baryonic mass, but with progenitor galaxies that are built up of a stellar bulge in addition to a gas-rich disk, each contributing half of the baryonic mass (*red*). Secular formation processes to grow such a bulge by coalescence of clumps in gas-rich disks (i.e., without invoking additional merging) have recently been proposed by Genzel et al. (2008), Elmegreen, Bournaud & Elmegreen (2008, and Dekel et al. (2009b)). We find that merging the bulge+disk systems leads to a compact ( $r_{e,V_{\text{rest}}} = 1$  kpc) remnant with significantly smoother central profile, but the strong wings remain in place. Analyzing its mock observations with GALFIT

yields a locus in  $(n, r_e)$ -space that does not overlap with the vD08 sample (see Figure 14b).

The same conclusion can be drawn from a third and fourth variation where we increase the disk dispersion twofold (*orange*) and adjust the merger mass ratio from equal mass to 1:3 (*blue*) respectively. The latter variations are inspired by the small  $\frac{v}{\sigma} = 2 - 4$  ratios of star-forming disk galaxies at  $z \sim 2$  observed by the SINS survey (Förster Schreiber et al. 2009), and by the paucity of equal-mass mergers compared to mergers of mass ratio 1:3 (Naab et al. 2007; Guo & White 2008; Hopkins et al. 2010b). We do not consider smaller mass ratios as they would not quench the star formation and produce a quiescent spheroid.

Finally, we considered the effect of adopting a lower pressurization of the ISM ( $q_{EOS} = 0.35$  instead of  $q_{EOS} = 1$  in the nomenclature of Springel, Di Matteo & Hernquist 2005). This leads to enhanced star formation in the outer regions during the early stages of the merging process, resulting in more pronounced wings in the remnant. This is in qualitative agreement with Bournaud et al. (2010) who find that the remnants of mergers of clumpy disks are cuspier (i.e., have higher Sérsic indices and more material at large radii) than those produced by merging disks in which the effective ISM is not allowed to fragment so completely.

Overall, the considered variations in progenitor properties have only a modest impact on the structure of the merger remnants: they occupy a similar region in the size-mass diagram, and have  $M/L$  ratio gradients that translate into similar color gradients (i.e., red cores; the dashed and solid lines in Figure 14a indicate the rest-frame  $U$  and  $V$  half-light radii respectively). Moreover, whereas the amplitude of the central cusp shows a dependence on the specific variations in progenitor structure explored here, the extended outskirts of the light distribution are present in each of the above model variations. As discussed in Section 7, a wider exploration of parameter space, involving physics leading to relative changes in the star formation efficiency between low- and high-density environments, may be appropriate to structurally alter the outer regions of the merger remnants.

### 6.3. The impact of subsequent merging

In this section, we address whether subsequent merging can alter the structure of the simulated merger remnants in such a way that their profile shape shows a closer resemblance to that of observed quiescent galaxies. To this extent, we run a set of re-merger simulations in which the remnant of the initial gas-rich merger collides with a star-forming galaxy of lower mass. We consider mass ratios 1:6 to 1:2, and initial gas fractions of 80%, 40% and 5% for the star-forming galaxies with which the merger remnant interacts. The resulting surface mass densities are presented in Figure 15. A more extended analysis, involving merger rates as function of mass, mass ratio, redshift and (redshift-dependent) gas fraction is required to properly model spheroid evolution (Khochfar & Silk 2006b; Naab et al. 2009; Hopkins et al. 2010a), but for our present purpose it is sufficient to highlight two characteristic features notable in our re-merger simulations.

First, the re-merger is consistently larger than the original merger remnant. The relation between the half-mass radius before and after depends on the nature (mass ra-

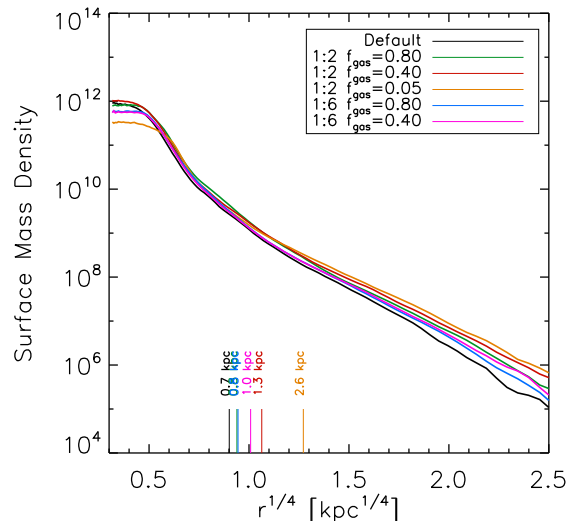


FIG. 15.— Surface mass density profile of a gas-rich merger remnant (*black*), and the products after re-merging it with star-forming galaxies of varying mass and initial gas fraction (*colored curves*). Half-mass radii are indicated by the vertical lines. Subsequent merging of a compact gas-rich merger remnant leads to a further build-up of its outer regions while the central dense cusp is little affected. This leads to an increase of the size, an effect that is most pronounced when the amount of dissipation is minimal.

tio, gas fraction, ...) of the re-merger. As expected, the size growth is larger for the 1:2 than for the 1:6 mass ratios. At a given mass ratio, the growth is more pronounced when the amount of dissipation is minimized (i.e., dry merging is more efficient at expanding galaxies).

Second, the re-merger remnant is not homologous to the original gas-rich merger remnant (see also Hopkins et al. 2009c; Hopkins & Hernquist 2010). Typically, we see the build-up of an outer wing while the dense central cusp is only little affected. This effect is more pronounced as we consider re-mergers with a lower dissipational fraction. The net effect is that, if anything, higher values of  $n$  are preferred in fitting the products of subsequent merging. In addition, their size at a given mass grows too big to be consistent with the observed spheroids at  $z \sim 2$ . While subsequent (minor) mergers might well drive the structural evolution of spheroids from  $z \sim 2$  to the present day (Naab et al. 2009; van Dokkum et al. 2010; Hopkins et al. 2010a; Carrasco et al. 2010), they are not a viable mechanism to produce the  $z \sim 2$  compact galaxies in the first place. Even if such an external process would yield sizes and profile shapes that matched the observations, it would not have offered a satisfactory solution, since it is unlikely that every quiescent galaxy observed at  $z \sim 2$  experienced a second interaction after the initial quenching event.

### 6.4. Stellar mass loss

In light of the last comment, it is interesting to consider internal, rather than external, processes that may alter the light distribution. One such process is stellar mass loss. The simulations presented in this paper were run with GADGET-2's default settings that account for a small amount of mass loss. Ten percent of the gas mass converted into stars is instantaneously returned to the interstellar medium (ISM, Springel & Hernquist 2003).

With it, energy is injected in the surrounding ISM to model the effect of short-lived stars that explode as supernovae. For currently favored stellar initial mass functions (IMFs) such as a Kroupa (2001) or Chabrier (2003) IMF, however, eventually as much as half of the gas mass initially converted into stars is returned to the ISM. Initially, the mass loss proceeds fast and in an explosive fashion, reaching 10% in 7 Myr and 25% in 60 Myr. At later times, AGB stars drive more gradual winds, increasing the released fraction to  $\sim 40\%$  after a gigayear (Bruzual & Charlot 2003). In principle, three things can happen to the mass lost due to winds: either it escapes the galaxy’s potential entirely, or it settles within the galaxy and stays there as gas, or it is consumed by star formation again. In addition, the redistribution of baryonic mass due to mass loss can potentially change (lower) the central potential, causing the distribution of stars to adjust (expand) accordingly. Fan et al. (2008) propose such a scenario of adiabatic expansion due to mass loss driven by AGN and/or stellar feedback as a mechanism for spheroid growth between  $z \sim 2$  and  $z \sim 0$ . Others (Bezanson et al. 2009; van Dokkum et al. 2010; Hopkins et al. 2010a) have objected to this process as a driver of structural evolution since  $z \sim 2$ , amongst other reasons because most of the mass loss is expected to take place within 500 Myr after the stars are formed, i.e., prior to the phase when the galaxies are observed as being quiescent. The same timescale argument works in favor of our present discussion. If mass loss modifies the surface brightness profile substantially, it will have happened by the time we observe the galaxies as being quiescent.

The precise effect of such extensive mass loss is however not trivial to predict, as the energetics, the amount of mass loss, and the location of the stars when they lose mass all depend on time. Moreover, the timescales of stellar evolution (i.e., mass loss), star formation history of the system, and merger dynamics all overlap. It will be interesting to investigate in future numerical work how a time-dependent treatment of extensive stellar mass loss and its feedback affects the outcome of simulations as the ones studied here. Since this is beyond the scope of this paper<sup>3</sup>, we now limit ourselves to simple toy models addressing the impact of, e.g., feedback on how the simulated quiescent galaxies would be observed.

#### 6.5. *Feedback, radiative transfer, and preventing star formation at early times*

In these toy models, we apply a simple transformation to a simulation snapshot of a merger remnant: an expansion by a fixed factor of the central component where the young stars dominate (Figure 16a), and additional extinction that decreases (Figure 16c) or increases (Figure 16e) with radius. The first toy model may be thought of as an ad hoc implementation of feedback, whereas the latter two explore dramatic differences in the effect of radiative transfer. The corresponding diagrams of recovered Sersic index versus recovered size when feeding mock NIC2 observations of the toy models to GALFIT are presented in the right-hand panels.

<sup>3</sup> We did test that, ignoring any time dependence of mass loss, increasing the fraction of material instantaneously returned to the ISM from 10% to 25% barely changes the surface brightness profile of the remnant.

The color-coding traces the expansion or extinction factor, where the legend quotes the extinction at  $r^{1/4} = 0.5$  kpc<sup>1/4</sup> and  $r^{1/4} = 1.5$  kpc<sup>1/4</sup> for the radially decreasing and increasing extinction respectively.

Figure 16(b) shows that, if a physical mechanism that is currently not or improperly modeled is capable of puffing up the central stellar cusp by over an order of magnitude, the best-fit Sersic indices enter the regime of those of the observed compact galaxies. However, the same transformation would lead to a violation of the observational constraints on size by a factor of several.

Likewise, larger sizes are inferred from toy model images where the central region is heavily obscured (Figure 16d). Moreover, as we already noted in the case of merging bulge+disk progenitors (§6.2), a reduction of the central cusp without any change to the outer wings does not necessarily lower the Sersic index inferred from the mock observations of limited depth and resolution.

A better correspondence with the locus of the vD08 sample in  $(n, r_e)$ -space is obtained when we lower the amplitude of the profile wings (Figure 16e). The plotted transformations reduce the true half-light radius (vertical lines in Figure 16e) by a factor 2 to 7, but the sizes inferred by GALFIT are of order 1 kpc. Although these toy models have observed properties similar to the vD08 galaxies, the required transformation factors are large (an order of magnitude or more) and it is hard to think of a radiative transfer effect related to the dust distribution or intrinsic stellar population properties in the wings that can account for such a deviation from our fiducial model.

There is another way of interpreting the last toy model. The outskirts are built up of old stars that formed in the progenitor disks and were redistributed by violent relaxation during the merger. Consequently, limiting the amount of star formation at early times may lower the amplitude of the wings. In the binary merger simulations considered here, this is hard to accomplish since all gas is already present at the start of the simulation and the compact gas-rich disks are sensitive to gravitational instabilities giving rise to star formation. This is the case even for the fully-pressurized multiphase ISM model adopted throughout this paper ( $q_{\text{EOS}} = 1$ ). A way to circumvent this problem would be to delay the supply of gas or spread it more continuously over time. Indeed, recent cosmological simulations suggest that galaxies during the first 3 billion years after the Big Bang were not closed systems, and supply of gas through cold filaments and streams was a generic feature of their evolution (Keres et al. 2005; Dekel & Birnboim 2006; Ocvirk et al. 2008; Dekel et al. 2009a). As such, reproducing not only the stellar population properties and size-mass relation, but also the profile shape of high-redshift quiescent galaxies may require simulations in a cosmological setting. This is numerically very challenging as a high spatial and timestep resolution (see §2.1) remain essential to model the detailed structure of the merger remnants, as well as the accretion processes onto the supermassive black hole(s) that contribute to the quenching of their star formation. Consequently, a resimulation technique (see, e.g., Tormen, Bouchet & White 1996) may be appropriate, as applied for example by Naab et al. (2007, 2009) in the context of spheroid formation.

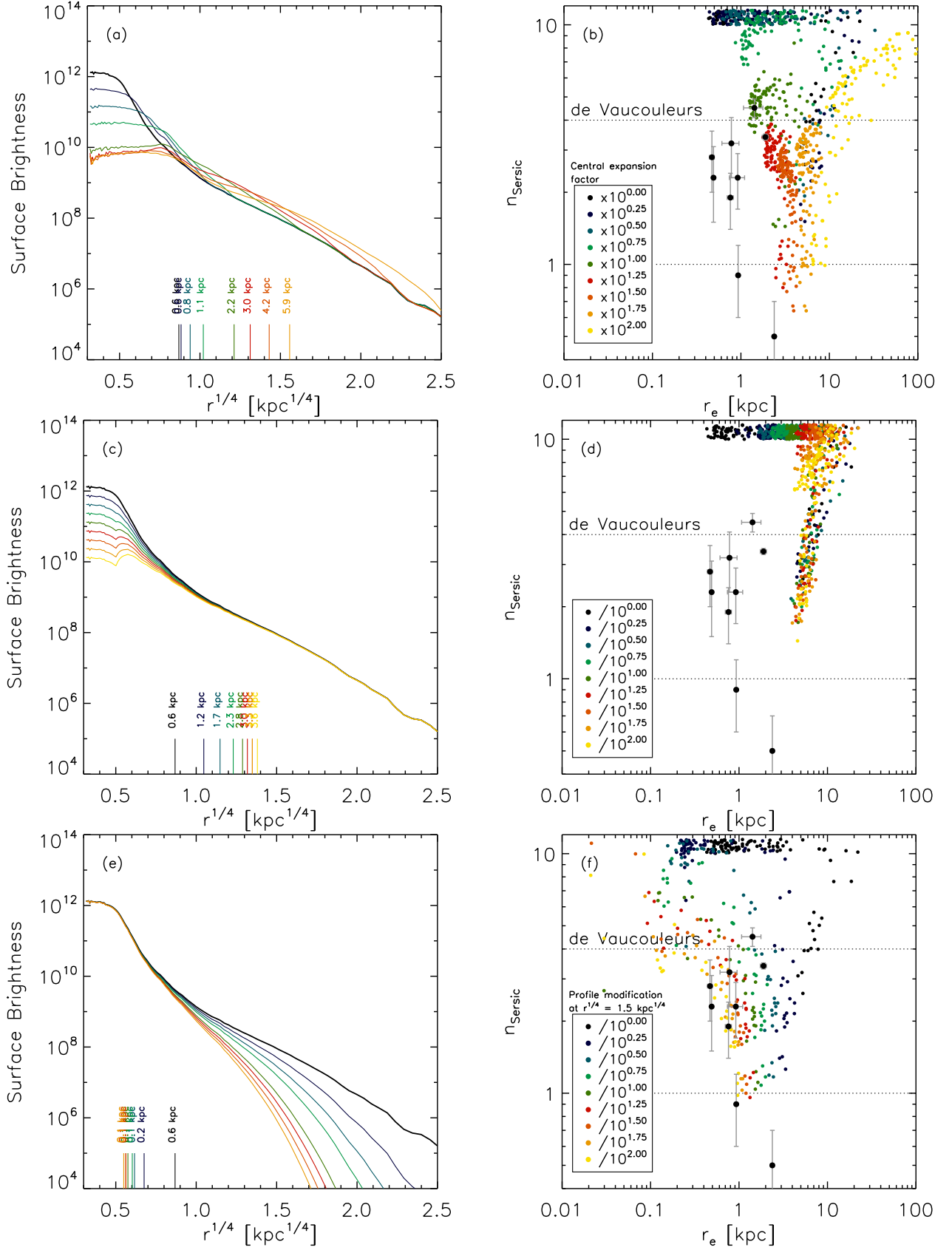


FIG. 16.— Idem as Figure 12, but for three toy models where we apply a simple transformation to a snapshot from a fiducial simulated merger remnant: (a-b) an expansion of the central region, (c-d) radially decreasing extinction, (e-f) radially increasing extinction. The high Sersic indices preferred in fitting the two-dimensional surface brightness profiles are driven by both the central cusp and the amount of light emerging from the extended wings of the profile. Only adjusting the central profile shape (a-d) is insufficient to match the vD08 galaxies in  $(n, r_e)$ -space. A mechanism to reduce the amount of stars at large radii (typically formed in the progenitors long before final coalescence), or the amount of light emerging from them seems required.

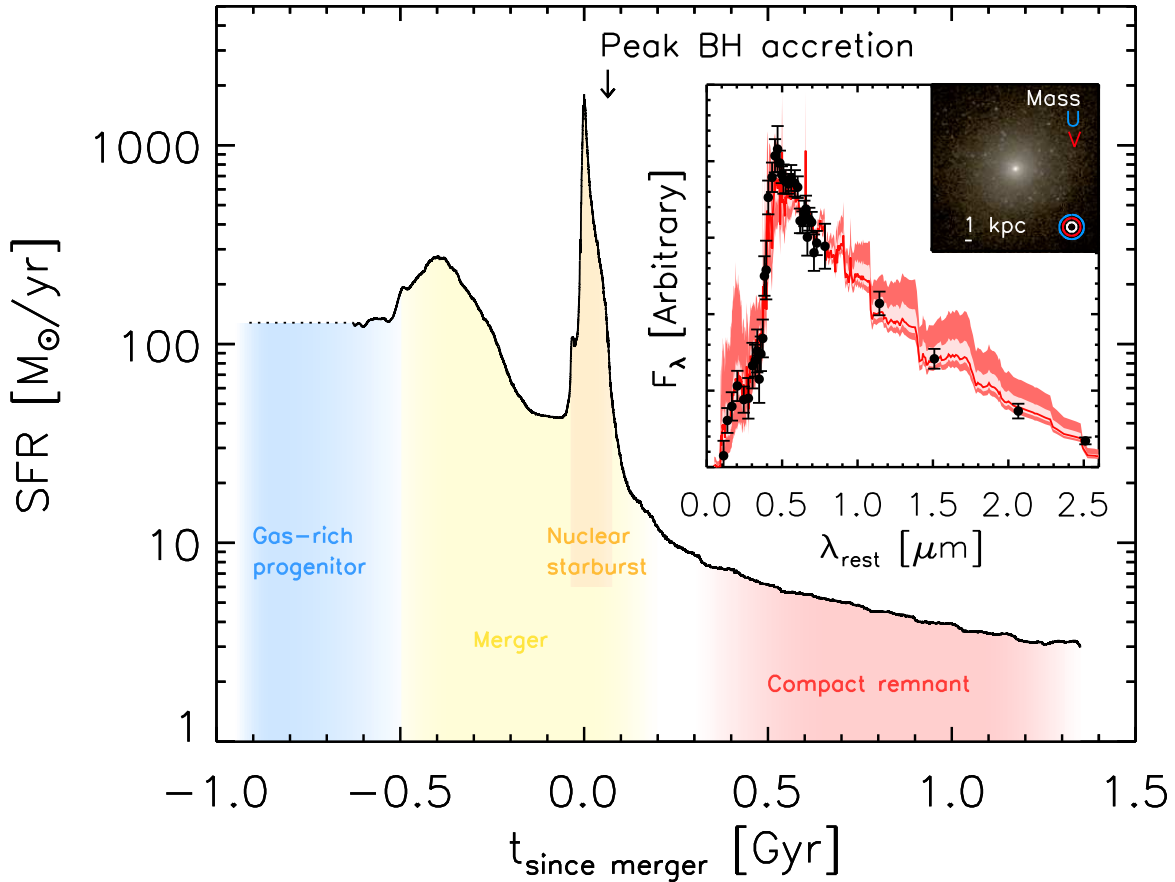


FIG. 17.— Star formation history of a gas-rich merger simulation producing a compact remnant. The spectral energy distribution (SED) of simulated remnants (*red in inset panel*) provides a good match to the mean SED of the observed compact quiescent galaxies from vD08. White, blue and red circles in the log-scaled postage stamp show the circularized region containing half the total mass,  $U$ - and  $V$ -band light respectively. A mass-to-light ratio gradient is present in the simulated remnant, which typically results in larger half-light radii at shorter wavelengths.

## 7. DISCUSSION AND SUMMARY

The existence of ultra-compact, massive ( $\sim 10^{11} M_{\odot}$ ) quiescent galaxies already in place merely 3 billion years after the Big Bang has been one of the great surprises of galaxy evolution studies in the last few years. Their discovery has triggered questions regarding their origin and fate, as well as the reliability with which their properties such as mass and size are characterized.

In this paper, we address the formation and nature of such systems in the context of (gas-rich) merger scenarios. As such, this study is part of a larger effort that couples hydrodynamic simulations with radiative transfer in order to investigate how different types of observed high-redshift galaxies may tie together as stages of one evolutionary sequence. Figure 17 illustrates a typical star formation history of a gas-rich merger simulation. Gas-rich star-forming galaxies (*blue*) are abundantly present at high redshift (Erb et al. 2006; Tacconi et al. 2010). When in the process of merging (*yellow*), the morphology of such systems may (but will not always) appear disturbed. The timescales of a morphological merger signature depend on mass ratio (Lotz et al. 2010a) and gas fraction (Lotz et al. 2010b) of the merger. Narayanan et al. (2010) describe how during a relatively short ( $< 50$  Myr) period at final coalescence (*orange*) a peak in emission at sub-millimeter wavelengths is reached. Continuing over a somewhat longer ( $\sim 100$  Myr) timespan, the

system may be identified as a so-called dust-obscured galaxy (DOG), characterized by its large  $24 \mu\text{m}$  to optical flux ratio, although not every DOG, and particularly those with low  $24 \mu\text{m}$  luminosity, is a gas-rich merger (Narayanan et al. 2009). Shortly after the peak in star formation rate (at  $t_{\text{since}} = 64$  Myr for the particular simulation shown), the accretion rate onto the central supermassive black hole peaks. The role of merging in galaxy - black hole coevolution has been discussed extensively by Hopkins et al. (2006, 2008a). Finally, Wuyts et al. (2009b) investigated the role major mergers may have played in producing the above mentioned compact systems, in terms of their number and mass densities as well as their integrated stellar population properties. Iterating on the latter aspect, the inset panel in Figure 17 contrasts the distribution of rest-frame UV to near-infrared SEDs of merger remnants computed from our simulations (*median, 50th and 100th percentiles are displayed in red*) to the mean rest-frame SED of quiescent galaxies from the vD08 sample (Muzzin et al. 2009b, *black data points, with error bars representing the error on the mean*). The model and observations show an excellent agreement over the full wavelength range probed, boosting confidence that the modeled stellar populations reflect reality at least in an integrated sense.

In this paper, we focussed on the structure and resolved stellar populations of merger remnants. We used



the sample of massive quiescent galaxies from vD08 as reference sample. Their near-infrared spectra are characterized by a Balmer/4000Å break (Kriek et al. 2006). Deep NIC2 observations (vD08) have revealed their compact nature at the highest resolution currently available. Analyzing a suite of binary merger simulations of varying mass, gas fraction, progenitor scaling, and orbital configuration, we confirm the idea originally proposed by Khochfar & Silk (2006a) that major mergers can explain their location in the size-mass diagram provided they are gas-rich. Merging galaxies scaled to represent high-redshift star-forming disks, we find that systems of  $\sim 10^{11} M_{\odot}$  with half-mass radius  $\sim 1$  kpc can be formed when the gas fraction by the time of final coalescence is about  $\sim 40\%$ . Observational evidence for gas fractions of this magnitude has been accumulating in recent years (e.g., Tacconi et al. 2010). The corresponding velocity dispersions of these simulated massive compact galaxies are of order 300 - 400 km s $^{-1}$ . They show considerable rotation ( $v_{\text{maj}}/\sigma$  of up to unity) compared to the majority of lower redshift early-type galaxies, a result that has yet to be confirmed observationally.

Running radiative transfer on the output of our SPH simulations, we find that the merger remnants have a radially dependent mass-to-light ratio. Typically, when observing the remnant 500 Myr to 1 Gyr after the peak in star formation rate, the half-mass radius is a factor  $\sim 2$  smaller than the rest-frame  $V$ -band half-light radius. This implies that the high effective densities inferred from NICMOS and WFC3 observations of high-redshift quiescent galaxies may in fact only be lower limits. In the rest-frame  $U$ -band, the typical light-to-mass size ratio increases to a factor 3-4. The ratio  $r_{e,\text{light}}/r_{e,\text{mass}}$  shows a significant sightline-dependence, with a tail to high values ( $\gtrsim 5$ ). Our conclusions are robust to the choice of radiative transfer code, input stellar population synthesis models, dust attenuation law, and whether or not the progenitor disks had stellar population gradients. The  $M/L$  ratio gradient is expressed as a color gradient that correlates with the integrated color of the system (redder galaxies hosting a more pronounced red core). We caution that the presence of a red core cannot unambiguously be interpreted as evidence for inside-out growth. In fact, in the simulations studied in this paper, the central stellar population formed last, rather than first. The effect of the negative age gradient is compensated by the fact that the stars inside the half-mass radius are more metal-rich, and suffer more extinction.

Finally, we perform two-dimensional parametric fitting with the GALFIT code (Peng et al. 2002) on real and mock NIC2 observations with the same limitations of resolution and depth. We find that our simulated merger remnants occupy a different region in  $(n, r_e)$ -space than the vD08 quiescent galaxies. So do simulations of disk galaxies that are left to evolve in isolation. The high Seric indices ( $n \gg 4$ ) inferred from the mock observations are driven by both the central cusp (consisting of young stars) and the extended wings (consisting of old stars). We explored a number of variations in progenitor properties that influence the amplitude of the central cusp, but have little effect on the outskirts. Subsequent (minor) merging tends to build up the profile wings even further while leaving the central cusp in the mass distribution relatively unaffected.

By lack of cosmological context, the binary merger simulations start with large amounts of gas in the progenitor disks (up to 80% of the baryonic mass content) in order to have a sufficiently large gas fraction by final coalescence to model the dissipational merger event. Given this large gas reservoir at the start of the simulation, it is hard to prevent it from forming stars and ending up forming the extended wings of the remnant profiles (wings that are not seen to that degree in the observations). As a consequence, while gas-rich mergers as simulated in this paper reproduce the basic structural diagnostic (the size-mass diagram), second order structural properties such as profile shape may differ because too many stars are formed at early times. This could be prevented if the gas was not all present initially but instead accreted more gradually over time, or if star formation and/or stellar mass loss and its feedback operated in such a way that the efficiency of converting gas into stars was lower at low densities than assumed here (i.e., in the progenitor disks and particularly their outer parts). One could speculate that a low gas-phase metallicity, turbulence from accretion (Bournaud et al. 2010), or the elevated intensity of the ionizing background radiation at  $z \sim 2$  inhibit the formation of molecular gas and thus stars during this early phase, especially at low densities where the gas may still be pristine.

We demonstrate that, in addition to spatial resolution, timestep resolution is important in modeling the detailed structure of such extreme systems properly. Therefore, running spheroid evolution simulations in a full cosmological context is computationally very expensive. Pioneering efforts to simulate spheroid formation in a cosmological context (without AGN feedback) have recently been carried out by Naab et al. (2007; 2009). These authors apply a resimulation technique on three target halos extracted from a low-resolution dark matter simulation to follow the formation and evolution of spheroids within those halos from high redshift to the present day. In agreement with our findings, Naab et al. (2007; 2009) argue that at high redshift dissipational processes on short timescales are a plausible mechanism to produce the compact galaxies observed at  $z \sim 2$ . At later times, they find that minor and gas-poor merging forms an efficient means to build up an envelope around this core (see also Section 6.3 of this paper, and Hopkins et al. 2009a).<sup>4</sup>

In the scenario investigated in this paper, the initial dissipational event occurs in the form of a major merger. Such a scenario connects three types of galaxies observed at high redshift in one evolutionary sequence: gas-rich disks, dusty starbursts with star formation rates peaking to  $\sim 1000 M_{\odot}/\text{yr}$ , and quiescent remnants. The dissipational event modeled by Naab et al. (2007; 2009) is driven by efficient radiative cooling and collapsing of gas, not necessarily involving major merging. It remains to be seen whether such a model can account for the peak star formation rates observed in, e.g., sub-millimeter galaxies, and the post-starburst nature of the stellar populations of compact galaxies. Observationally, measurements of

<sup>4</sup> In detail, as noted already by Naab et al. (2009), their simulated spheroid with size  $r_e = 2.4 \pm 0.4$  kpc and mass  $M = 1.5 \times 10^{11} M_{\odot}$  lies in the low tail of the size distribution of observed nearby galaxies with similar mass.

clustering, from large scales to pair counts, based on wide and deep cosmological surveys could potentially provide support for a merger-driven evolutionary scenario.

S. Wuyts and P. Jonsson gratefully acknowledge support from the W. M. Keck Foundation.

## REFERENCES

- Baker, A. J., Tacconi, L. J., Genzel, R., Lehnert, M. D., & Lutz, D. 2004, *ApJ*, 604, 125
- Barnes, J. E., Hernquist, L. 1991, *ApJ*, 370, L65
- Barnes, J. E. 1992, *ApJ*, 393, 484
- Barnes, J. E., Hernquist, L. 1996, *ApJ*, 471, 115
- Bezanson, R., van Dokkum, P. G., Tal, T., Marchesini, D., Kriek, M., Franx, M., & Coppi, P. 2009, *ApJ*, 697, 1290
- Binney, J. 1978, *MNRAS*, 183, 501
- Binney, J., & Merrifield, M. 1998, *Galactic Astronomy*, Princeton University Press, Princeton
- Bournaud, F., et al. 2010, submitted to *ApJL* (astro-ph 1006.4782)
- Bruzual, G., & Charlot, S. 2003, *MNRAS*, 344, 1000
- Buitrago, F., Trujillo, I., Conselice, C. J., Bouwens, R. J., Dickinson, M., & Yan, H. 2008, *ApJ*, 687, L61
- Bullock, J. S., Kolatt, T. S., Sigad, Y., Somerville, R. S., Kravtsov, A. V., Klypin, A. A., Primack, J. R., & Dekel, A. 2001, *MNRAS*, 321, 559
- Cappellari, M., et al. 2006, *MNRAS*, 366, 1126
- Cappellari, M., et al. 2009, *ApJ*, 704, L34
- Carrasco, E. R., Conselice, C. J., & Trujillo, I. 2010, *MNRAS*, in press (astro-ph 1003.1956)
- Cenarro, A. J., & Trujillo, I. 2009, *ApJ*, 696, L43
- Chabrier, G. 2003, *PASP*, 115, 763
- Cimatti, A., et al. 2008, *A&A*, 482, 21
- Coppin, K. E. K., et al. 2007, *ApJ*, 665, 936
- Cox, T. J., Dutta, S. N., Di Matteo, T., Hernquist, L., Hopkins, P. F., Robertson, B., & Springel, V. 2006, *ApJ*, 650, 791
- Daddi, E., et al. 2005, *ApJ*, 626, 680
- Daddi, E., Dannerbauer, H., Elbaz, D., Dickinson, M., Morrison, G., Stern, D., & Ravindranath, S. 2008, *ApJ*, 673, L21
- Davé, R. 2008, *MNRAS*, 385, 147
- Dekel, A., & Birnboim, Y. 2006, *MNRAS*, 368, 2
- Dekel, A., et al. 2009a, *Nature*, 457, 451
- Dekel, A., Sari, R., & Ceverino, D. 2009b, *ApJ*, 703, 785
- Di Matteo, T., Springel, V., & Hernquist, L. 2005, *Nature*, 433, 604
- Di Matteo, P., Pipino, A., Lehnert, M. D., Combes, F., & Semelin, B. 2009, *A&A*, 499, 427
- Elmegreen, B. G., Bournaud, F., Elmegreen, D. M. 2008, *ApJ*, 688, 67
- Erb, D. K., Steidel, C. C., Shapley, A. E., Pettini, M., Reddy, N. A., & Adelberger, K. L. 2006, *ApJ*, 646, 107
- Fan, L., Lapi, A., De Zotti, G., & Danese, L. 2008, *ApJ*, 689, L101
- Förster Schreiber, N. M., et al. 2009, *ApJ*, 706, 1364
- Franx, M., van Dokkum, P. G., Förster Schreiber, N. M., Wuyts, S., Labbé, I., & Toft, S. 2008, *ApJ*, 688, 770
- Genzel, R., et al. 2008, *ApJ*, 687, 59
- Groves, B., Dopita, M. A., Sutherland, R. S., Kewley, L. J., Fischera, J., Leitherer, C., Brandl, B., & van Breugel, W. 2008, *ApJS*, 176, 438
- Guo, Q., & White, S. D. M. 2008, *MNRAS*, 384, 2
- Jonsson, P. 2006, *MNRAS*, 372, 2
- Jonsson, P., Groves, B., & Cox, T. J. 2010, *MNRAS*, 403, 17
- Hernquist, L. 1990, *ApJ*, 356, 359
- Hopkins, P. F., Hernquist, L., Martini, P., Cox, T. J., Robertson, B., Di Matteo, T., & Springel, V. 2005, *ApJ*, 625, L71
- Hopkins, P. F., Hernquist, L., Cox, T. J., Di Matteo, T., Robertson, B., & Springel, V. 2006, *ApJS*, 163, 1
- Hopkins, P. F., Hernquist, L., Cox, T. J., Keres, D. 2008a, *ApJS*, 175, 356
- Hopkins, P. F., Hernquist, L., Cox, T. J., Dutta, S. N., & Rothberg, B. 2008b, *ApJ*, 679, 156
- Hopkins, P. F., Cox, T. J., & Hernquist, L. 2008, *ApJ*, 689, 17
- Hopkins, P. F., Hernquist, L., Cox, T. J., Keres, D., & Wuyts, S. 2009a, *ApJ*, 691, 1424
- Hopkins, P. F., Cox, T. J., Dutta, S. N., Hernquist, L., Kormendy, J., & Lauer, T. R. 2009b, *ApJS*, 181, 135
- Hopkins, P. F., Lauer, T. R., Cox, T. J., Hernquist, L., & Kormendy, J. 2009c, *ApJS*, 181, 486
- Hopkins, P. F., Bundy, K., Murray, N., Quataert, E., Lauer, T. R., & Ma, C.-P. 2009d, *MNRAS*, 398, 898
- Hopkins, P. F., Bundy, K., Hernquist, L., Wuyts, S., & Cox, T. J. 2010a, *MNRAS*, 401, 1099
- Hopkins, P. F., et al. 2010b, *ApJ*, 715, 202
- Hopkins, P. F., & Hernquist, L. 2010, *MNRAS*, in press (astro-ph 1006.0488)
- Keres, D., Katz, N., Weinberg, D. H., & Davé, R. 2005, 363, 2
- Khochfar, S., & Silk, J. 2006a, *ApJ*, 648, L21
- Khochfar, S., & Silk, J. 2006b, *MNRAS*, 370, 902
- Kriek, M., et al. 2006, *ApJ*, 649, 71
- Kroupa, P. 2001, *MNRAS*, 322, 231
- Kuntschner, H., et al. 2010, *MNRAS*, in press (astro-ph 1006.1574)
- Labbé, I., et al. 2005, *ApJ*, 624, L81
- Lotz, J. M., Jonsson, P., Cox, T. J., & Primack, J. R. 2010a, *MNRAS*, 404, 575
- Lotz, J. M., Jonsson, P., Cox, T. J., & Primack, J. R. 2010b, *MNRAS*, 404, 590
- Maraston, C. 2005, *MNRAS*, 362, 799
- Maraston, C., Daddi, E., Renzini, A., Cimatti, A., Dickinson, M., Papovich, C., Pasquali, A., & Pirzkal, N. 2006, *ApJ*, 652, 85
- Mihos, J. C., Hernquist, L. 1994, *ApJ*, 431, L9
- Mihos, J. C., Hernquist, L. 1996, *ApJ*, 464, 641
- Mo, H. J., Mao, S., & White, S. D. M. 1998, *MNRAS*, 295, 319
- Muzzin, A., van Dokkum, P. G., Franx, M., Marchesini, D., Kriek, M., & Labbé, I. 2009a, *ApJ*, 706, 188
- Muzzin, A., Marchesini, D., van Dokkum, P. G., Labbé, I., Kriek, M., & Franx, M. 2009b, *ApJ*, 701, 1839
- Naab, T., Jesseit, R., & Burkert, A. 2006, *MNRAS*, 372, 839
- Naab, T., Johansson, P. H., Ostriker, J. P., & Efstathiou, G. 2007, *ApJ*, 658, 710
- Naab, T., Johansson, P. H., & Ostriker, J. P. 2009, *ApJ*, 699, 178
- Narayanan, D., et al. 2009, *MNRAS*, in press (astro-ph 0910.2234)
- Narayanan, D., Hayward, C. C., Cox, T. J., Hernquist, L., Jonsson, P., Younger, J. D., & Groves, B. 2010, *MNRAS*, 401, 1613
- Ocvirk, P., Pichon, C., & Teyssier, R. 2008, *MNRAS*, 390, 13260
- Paturel, G., et al. 2003, *A&A*, 412, 45
- Peng, C. Y., Ho, L. C., Impey, C. D., & Rix, H.-W. 2002, *AJ*, 124, 266
- Peirani, S., Crockett, R. M., Geen, S., Khochfar, S., Kaviraj, S., & Silk, J. 2010, *MNRAS*, 405, 2327
- Rawle, T. D., Smith, R. J., & Lucey, J. R. 2010, *MNRAS*, 401, 852
- Robertson, B., Cox, T. J., Hernquist, L., Franx, M., Hopkins, P. F., Martini, P., & Springel, V. 2006, *ApJ*, 641, 21
- Robertson, B., Li, Y., Cox, T. J., Hernquist, L., & Hopkins, P. F. 2007, *ApJ*, 667, 60

- Ryan, R. E., et al. 2010, submitted to ApJ (astro-ph 1007.1460)
- Sersic, J. L. 1968, Atlas de galaxias australes (Cordoba, Argentina: Observatorio Astronomico, 1968)
- Shen, S., Mo, H. J., White, S. D. M., Blanton, M. R., Kauffmann, G., Voges, W., Brinkmann, J., & Csabai, I. 2003, MNRAS, 343, 978
- Springel, V., & Hernquist, L. 2002, MNRAS, 333, 649
- Springel, V., & Hernquist, L. 2003, MNRAS, 339, 289
- Springel, V. 2005, MNRAS, 364, 1105
- Springel, V., Di Matteo, T., & Hernquist, L. 2005, MNRAS, 361, 776
- Szomoru, D., et al. 2010, ApJ, 714, L244
- Tacconi, L. J., et al. 2010, Nature, 463, 781
- Toft, S., et al. 2007, ApJ, 671, 285
- Tormen, G., Bouchet, F. R., & White, S. D. M., 1997, MNRAS, 286, 865
- Trujillo, I., et al. 2006, ApJ, 650, 18
- van der Wel, A., Holden, B. P., Zirm, A. W., Franx, M., Rettura, A., Illingworth, G. D., & Ford, H. C. 2008, ApJ, 688, 48
- van der Wel, A., & van der Marel, R. P. 2008, ApJ, 684, 260
- van Dokkum, P. G., & Stanford, S. A. 2003, ApJ, 585, 78
- van Dokkum, P. G., et al. 2006, ApJ, 638, 59
- van Dokkum, P. G. 2008, ApJ, 674, 29
- van Dokkum, P. G., et al. 2008, ApJ, 677, 5
- van Dokkum, P. G., Kriek, M., & Franx, M. 2009, Nature, 460, 717
- van Dokkum, P. G., et al. 2010, ApJ, 709, 1018
- Vitvitska, M., Klypin, A. A., Kravtsov, A. V., Wechsler, R. H., Primack, J. R., & Bullock, J. S. 2002, ApJ, 581, 799
- Wilkins, S. M., Hopkins, A. M., Trentham, N., & Tojeiro, R. 2008, MNRAS, 391, 363
- Williams, R. J., Quadri, R. F., Franx, M., van Dokkum, P., Toft, S., Kriek, M., & Labbé, I. 2010, ApJ, 713, 738
- Wuyts, S., et al. 2007, ApJ, 655, 51
- Wuyts, S., Franx, M., Cox, T. J., Hernquist, L., Hopkins, P. F., Robertson, B. E., & van Dokkum, P. G. 2009a, ApJ, 696, 348
- Wuyts, S., et al. 2009b, ApJ, 700, 799
- Younger, J. D., Hayward, C. C., Narayanan, D., Cox, T. J., Hernquist, L., & Jonsson, P. 2009, MNRAS, 396, 66
- Zirm, A. W., et al. 2007, ApJ, 656, 66